A COMPUTATIONAL FRAMEWORK FOR TRACKING GRAIN BOUNDARIES IN 3D IMAGE DATA: QUANTIFYING BOUNDARY CURVATURES AND VELOCITIES IN POLYCRYSTALLINE MATERIALS

THOMAS WILHELM[1], ORKUN FURAT[1,2], JULES M. DAKE[3],
CARL E. KRILL III[3], VOLKER SCHMIDT[1]

[1]*Institute of Stochastics, Ulm University, 89069 Ulm, Germany*

[2]*SDU Applied AI and Data Science Unit, University of Southern Denmark,
Campusvej 55, 5230 Odense, Denmark*

[3]*Institute of Functional Nanosystems, Ulm University, 89081 Ulm, Germany*

Abstract. Diffraction-based methods for 3D microstructure mapping have revolutionized the investigation of grain growth phenomena in polycrystalline materials. These techniques provide unprecedented experimental access to the location, shape and migration of individual grain boundaries in real samples, together with other relevant boundary parameters, such as misorientation and inclination. However, achieving the ultimate goal of such studies — the identification of physical mechanisms responsible for the observed evolution of microstructure — is impeded by the voxel-based representation of microstructure intrinsic to 3D mapping. The staircase-like discretization of grain boundaries complicates the determination of boundary positions and local curvatures, motivating a transition from a discrete to a continuous representation of the boundary network. This paper introduces an approach based on smoothing thin-plate splines with radial basis functions to represent grain boundaries as continuous surfaces. The method can approximate arbitrarily shaped boundaries while preserving local mean curvatures and, for time-resolved series of images, local boundary velocities. Its accuracy is validated against two datasets: a multiplicatively weighted Laguerre tessellation, where mean curvatures are known analytically, and a Reuleaux tetrahedron evolving under a phase field model, for which local boundary velocities can be determined exactly. The applicability of the method to experimental data is demonstrated using time-resolved 3D maps of grain growth in an Al–Mg alloy.

Keywords: polycrystalline material; kinetics of grain growth; spline; radial basis function; 3D microstructure mapping; 3DXRD microscopy

1. **Introduction**

For more than a century, grain growth in polycrystalline materials has intrigued researchers because of the profound impact of grain size on materials properties. Early investigations established that curved grain boundaries migrate toward their center of curvature [1], and Burke and Turnbull's analytic model [2] explained the parabolic relationship between the average grain size and annealing time during normal grain growth, under the assumption that the velocity v of a grain boundary is given by the product of its mobility M, excess energy per unit area γ and mean curvature H:

$$v = M\gamma H. \tag{1}$$

This equation provides a framework for simulating grain growth [3–14], with recently implemented algorithms capable of handling millions of grains, from which statistically robust measures for ensemble-averaged features of the microstructure can be extracted [15, 16]. However, despite these advances, discrepancies persist between experimental observations and model-based predictions. Modern experimental techniques, such as orientational imaging microscopy [17], automated serial sectioning [18, 19] and X-ray diffraction-based microscopy [20], have revealed shapes of grain size distributions as well as other aspects of microstructure evolution that current models do not accurately predict [21]. For example, a recent investigation of grain growth in polycrystalline Ni found that, for 35% of the grains in the sample, conventional growth models fail to predict the correct *sign* of a grain's volume change, let alone the detailed evolution of its shape [22].

Thus, it appears that current analytic and computational models for grain growth do not fully capture the complexities of the physics underlying grain boundary migration. Furthermore, early approaches considered solely the influence of the mean curvature H on microstructure evolution, associating each grain boundary with the same value of the parameters M and γ — a condition referred to as "ideal" grain growth. However, in real polycrystalline materials, the mobility and excess energy are known to vary from boundary to boundary and even from one region to another within a single boundary [23, 24]. These variations arise from the dependence of M on other parameters, such as the grain boundary misorientation θ [25,26] and the boundary inclination [27]. Values for M and γ are typically determined from bicrystal experiments [25,27], from measurements of grain boundary grooving [28] or from atomistic simulations [29–32]. However, all of these approaches suffer from the practical difficulty of properly sampling the high-dimensional parameter space of quantities on which M can depend.

Recently, an effort was initiated to extract the working principles of grain growth from experimentally acquired image datasets depicting the evolution of the grain boundary network in polycrystalline materials [33]. Because the approach works backward from measured effect to governing cause, the authors refer to their method as the *reverse engineering* of grain growth. The procedure relies on 3D X-ray diffraction (3DXRD) microscopy [34–36], which is used to map the microstructure of polycrystalline specimens nondestructively and in 3D. Time-resolved snapshots are acquired that track the migration of grain boundaries under isothermal annealing conditions. The resulting reconstructions constitute the basis for estimating the quantities v and H for each grain boundary. Inserting these values into Eq. (1), the product of M and γ — commonly called the *reduced mobility* $\widetilde{M}$ — can be determined from the relation

$$\widetilde{M} = M\gamma = \frac{v}{H}. \tag{2}$$

Imaging techniques such as 3DXRD microscopy typically generate maps of microstructures that are projected onto a grid of equispaced voxels. The discrete nature of such a voxel-based representation introduces intrinsic "granularity" that greatly complicates the accurate determination of grain boundary mean curvatures and their local velocities. To mitigate these issues, it is necessary to transition from a discrete to a continuous representation of microstructure.

Several methods have been explored to generate a continuous representation of grain boundaries — i.e., one in which each grain boundary is represented by a continuous function.

For polycrystalline materials, a common approach involves the use of distance-based tessellation models [37–43], which partition 3D space into distinct regions that parametrically represent the individual grains of a polycrystal. This method has the advantage of allowing for the analytic computation of mean curvature at each point on a grain boundary from the parametric representation. However, these parametric tessellation models provide limited flexibility in accurately fitting the morphology of individual grain boundaries, as the representations typically rely on low-order polynomial functions [44]. This constraint becomes particularly problematic for boundaries with shapes deviating significantly from low-order polynomial forms, resulting in overly smoothed and less realistic surface representations. Furthermore, when distance-based tessellation models are used to represent experimentally acquired image data of polycrystalline materials, the grain topology and, in particular, neighborhood relationships between adjacent grains are sometimes not preserved [45], potentially leading to a loss of grain boundaries during construction.

An alternative approach involves the use of surface meshing techniques to represent grain boundaries [33, 46]. This method has the advantage of making almost no model assumptions when representing grain boundaries, with meshes providing an accurate geometric representation of grain boundary structures extracted from image data. Surface meshing was used, for example, in Refs. [33] and [46] to determine values for the velocity and reduced mobility of grain boundaries from voxelized 3D image data.

In the present paper, we develop a computational approach — referred to as the *surface representation method* — that employs smoothing thin-plate splines [47, 48] based on radial basis functions [49–52] to represent each grain boundary as a continuous surface in 3D. This method provides an explicit representation of arbitrarily shaped, curved grain boundaries, thereby facilitating computation of the local mean curvature and velocity at each point on the grain boundary network. The proposed approach circumvents the problem of losing grain boundaries during the tessellation construction step, preserving all neighborhood relationships between grains. Assessment of the proposed approach is carried out with respect to three different datasets: First, the method is evaluated according to its accuracy in computing local mean curvatures of boundaries between the cells of a discretized multiplicatively weighted Laguerre tessellation. This type of tessellation can exhibit curved grain boundaries, which, in turn, can serve as continuous representations of experimentally acquired image data (under the assumption that the latter's grain boundaries are amenable to representation by polynomials). The advantage of constructing a test case around a multiplicatively weighted Laguerre tessellation is found in the fact that the *true* local mean curvature is known analytically at all points on the boundaries of the tessellation.

Secondly, we evaluate the accuracy with which the surface representation method estimates local boundary velocities and reduced mobilities. Here, we apply it to a discretized Reuleaux tetrahedron dataset [33, 53] that has been coarsened using a phase field simulation. Such a simulation generates time-resolved image data from known input parameters — in particular, from the boundary mobility M and the excess energy γ — thus fixing the value of the reduced mobility $\widetilde{M}$. By construction, the curved surfaces of the Reuleaux tetrahedron are spherical patches, exhibiting constant curvature. Thus, under the assumption of identical $\widetilde{M}$ at each point on the tetrahedron surface (a condition enforced by the simulation algorithm), we can draw on Eq. (1) to compute an analytic value for the boundary velocity v as a function of time, against which the output of the surface representation method can be validated.

Finally, we apply the method to time-resolved experimental 3DXRD image datasets obtained from an Al-1 wt% Mg (AlMg) alloy undergoing grain growth [54]. By representing grain boundaries as continuous surfaces using smoothing thin-plate splines, our approach provides a more robust and flexible tool than previous methods for studying microstructure evolution. Owing to its local accuracy, the new framework provides the mathematical foundation for assessing the influence of local variations in boundary curvature on the effective mobility of individual grain boundaries in polycrystalline materials. In turn, such findings have the potential to help resolve (apparent) discrepancies between the conventional picture of curvature-driven grain growth and recent reports of "anti-curvature" grain boundary migration [55] or migration partially or completely uncoupled from curvature [46, 56, 57].

2. Materials and image processing

In this section, the materials and image processing methods employed in the present paper are described. Topics include a description of the 3D image data in Section 2.1 and the extraction of grain boundaries from the image data in Section 2.2. For the sake of clarity, the most important mathematical symbols used in this paper are listed and explained in Appendix C.

2.1. **Description of 3D image data**

The objective of this paper is to describe a method to analyze the migration of points located on the grain boundaries of real experimental image data. The term *grain boundary* denotes the interface between adjacent grains of the same phase in a polycrystalline material. To extract such interfaces from image data, a formal definition of the image dataset is required: each image is defined as a mapping $I\colon W \to \{0, 1, 2, \ldots, n_G\}$, where the domain $W \subset \mathbb{Z}^3 = \{\ldots, -1, 0, 1, \ldots\}^3$ is given by $W = W' \cap \mathbb{Z}^3$ for a bounded cuboidal sampling window $W' \subset \mathbb{R}^3$, and $n_G \geq 1$ denotes the total number of grains in the domain. In this framework, the image I assigns each voxel $x \in W$ to a specific grain or the background — i.e., I is given by

$$I(x) = \begin{cases} i, & \text{if } x \text{ belongs to the } i\text{th grain for } i \in \{1, 2, \ldots, n_G\}, \\ 0, & \text{otherwise,} \end{cases} \tag{3}$$

for each $x \in W$. In the present paper, three datasets are considered. First, the surface representation method mentioned in the introduction is applied to a discretized version of a multiplicatively weighted Laguerre tessellation that had been fitted to an experimental dataset, as detailed in Section 2.1.1 below. Subsequently, our method is applied to two time-resolved datasets: initially, to a simulated single-grain dataset (Section 2.1.2), and, finally, to a sequence of 3D images representing the evolving microstructure of an AlMg alloy (Section 2.1.3).

2.1.1. ***Multiple-grain dataset: Multiplicatively weighted Laguerre tessellation.*** In order to generate a realistic multiple-grain dataset for model validation, we employ a multiplicatively weighted Laguerre tessellation, which is a special type of distance-based tessellation model [58] and a simplified version of a generalized balanced power diagram (GBPD) [59]. This tesselation model is fully specified by a marked point pattern given by

$$\mathcal{G} = \{(g_i, m_i, a_i) : i \in \{1, \ldots, n_{\mathcal{T}}\}\} \subset \mathbb{R}^3 \times \mathbb{R} \times \mathbb{R},$$

consisting of seed points g_i, multiplicative weights m_i and additive weights a_i for each $i \in \{1, \ldots, n_{\mathcal{T}}\}$, with the integer $n_{\mathcal{T}} \geq 1$ denoting the number of tessellation cells. The ith cell $C_i \subset \mathbb{R}^3$ of the multiplicatively weighted Laguerre tessellation $\mathcal{T} = \{C_i : i \in \{1, \ldots, n_{\mathcal{T}}\}\}$ is then defined as

$$C_i = \{x \in W'\colon \|x - g_i\|^2 m_i - a_i \leq \|x - g_j\|^2 m_j - a_j \text{ for each } j \in \{1, \ldots, n_{\mathcal{T}}\}\} \tag{4}$$

for some cuboidal sampling window $W' \subset \mathbb{R}^3$, where $\|\cdot\|$ denotes the Euclidean norm in $\mathbb{R}^3$. The boundaries between cells of the multiplicatively weighted Laguerre tessellation are patches of quadratic surfaces; that is, the boundary between two cells C_i and C_j is given by the set

$$C_{ij} = \{x \in C_i \colon \|x - g_i\|^2 m_i - a_i = \|x - g_j\|^2 m_j - a_j\}. \tag{5}$$

A discretized version $\mathcal{T}_\mathrm{d} = \{C_{\mathrm{d},i} : i \in \{1, \dots, n_\mathcal{T}\}\}$ of $\mathcal{T}$ is obtained by evaluating Eq. (4) on the lattice $W = W' \cap \mathbb{Z}^3$; that is, the ith (discretized) cell $C_{\mathrm{d},i}$ of $\mathcal{T}_\mathrm{d}$ is given by

$$C_{\mathrm{d},i} = \{x \in W \colon \|x - g_i\|^2 m_i - a_i \leq \|x - g_j\|^2 m_j - a_j \text{ for each } j \in \{1, \dots, n_\mathcal{T}\}\} \tag{6}$$

for each $i \in \{1, 2, \dots, n_\mathcal{T}\}$. In a voxelized image setting, the tessellation $\mathcal{T}_\mathrm{d}$ can be represented by an image $I_{\mathcal{T}_\mathrm{d}} \colon W \to \{0, 1, \dots, n_\mathcal{T}\}$, where for each $x \in W$ it holds that $I_{\mathcal{T}_\mathrm{d}}(x) = i$ if $x \in C_{\mathrm{d},i}$ for some $i \in \{1, 2, \dots, n_\mathcal{T}\}$. For the remainder of this paper, whenever we use tessellations to represent polycrystalline materials, we will refer to individual tessellation cells as grains and to the boundaries between adjacent cells as grain boundaries.

In this work, we consider a multiplicatively weighted Laguerre tessellation that had previously been fitted in Ref. [43] to 3DXRD data from an AlCu alloy [34]. In Figure 1(a), 2D slices of the experimentally acquired image data and the corresponding discretized version of the fitted multiplicatively weighted Laguerre tessellation are visualized.

2.1.2. ***Single-grain dataset: Reuleaux tetrahedron.*** A Reuleaux tetrahedron (see, e.g., Refs. [33,53,60]) is created by the intersection of four spheres of equal radius $r > 0$, positioned at the vertices $s_1, s_2, s_3, s_4 \in \mathbb{R}^3$ of a regular tetrahedron with side length r; the centerpoints of the four spheres are located at the vertices s_1, s_2, s_3, s_4. Here, the Reuleaux tetrahedron is formally defined as a subset of the continuous Euclidean space $\mathbb{R}^3$ contained in a cube $W' \subset \mathbb{R}^3$, where the surrounding space of the Reuleaux tetrahedron is partitioned into four surrounding regions of equal volume by placing planar boundaries along diagonals of the faces of the cubic observation window W' and extending each plane inwards until it intersects the Reuleaux tetrahedron along one of its edges, as described in Ref. [33]. An analytic representation of the Reuleaux tetrahedron with radius r is given by the set $R = \{x \in W' \colon \|x - s_i\| \leq r \text{ for each } i \in \{1, 2, 3, 4\}\}$. The boundary of R can be decomposed into four grain boundaries $R_i \subset R$ with $i \in \{1, 2, 3, 4\}$ corresponding to the boundaries of the four spheres centered at $s_1, s_2, s_3, s_4 \in \mathbb{R}^3$, where $R_i = \big\{x \in R \colon \|x - s_i\| = r\big\}$. A discretized version $R_\mathrm{d} \subset \mathbb{Z}^3$ of the Reuleaux tetrahedron is given by

$$R_\mathrm{d} = \{x \in W \colon \|x - s_i\| \leq r \text{ for each } i \in \{1, 2, 3, 4\}\}, \tag{7}$$

where $W = W' \cap \mathbb{Z}^3$. In the present paper, the discretized Reuleaux tetrahedron R_d is represented by an image $I_{R_\mathrm{d}} \colon W \to \{1, 2, 3, 4, 5\}$, which assigns each voxel in W either to the Reuleaux tetrahedron by the label five or to one of the surrounding four regions by the label i for the ith surrounding region, i.e., it holds that

$$I_{R_\mathrm{d}}(x) = \begin{cases} 5, & \text{if } x \in R_\mathrm{d}, \\ i, & \text{if } x \text{ belongs to the } i\text{th surrounding region,} \end{cases} \tag{8}$$

for any $x \in W$ and $i \in \{1, 2, 3, 4\}$. A visualization of the continuous and corresponding voxelized version of the Reuleaux tetrahedron with radius $r = 80$ is shown in Figure 1(b). (The four regions that surround the tetrahedron were omitted from the figure for clearer visualization.)

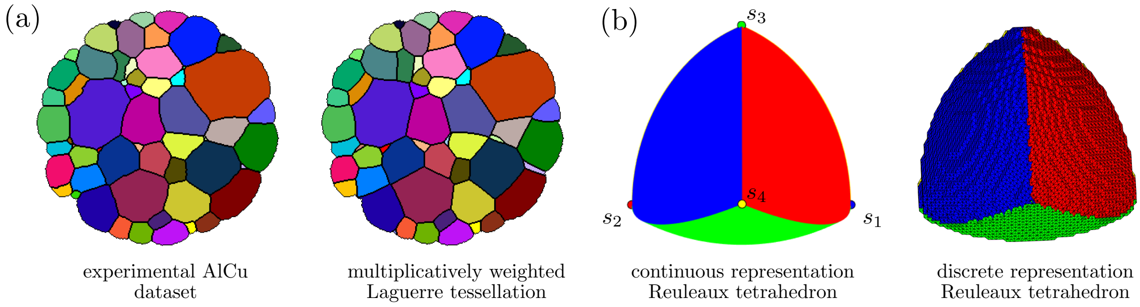

FIGURE 1. (a) 2D slice through a 3DXRD microscopy measurement of AlCu and the corresponding 2D slice of a discretized version of a multiplicatively weighted Laguerre tessellation fitted to the experimental dataset. (b) 3D rendering of the analytic representation of a Reuleaux tetrahedron in continuous Euclidean space $\mathbb{R}^3$ and its voxelized discretization. The color of each boundary of the Reuleaux tetrahedron matches the color of its corresponding sphere centerpoint $s_1, s_2, s_3, s_4 \in \mathbb{R}^3$.

2.1.3. ***Experimental dataset: Al-1 wt% Mg (AlMg) alloy.*** A key objective of this paper is to develop a method to analyze the local migration behavior of grain boundaries in experimental image data. To pursue this goal, 3D microstructure mapping was performed on a cylindrical AlMg specimen with a diameter of 1.4 mm, extracted from a cold-rolled plate via spark erosion. The plate had undergone a 50% reduction in thickness through cold rolling before the sample was recrystallized at 350 °C for 75 min. The 3D microstructure of the sample was mapped using 3DXRD microscopy at the BL20XU beamline of the SPring-8 synchrotron radiation facility in Japan. These measurements, subsequently reported in Ref. [54], were performed using an incident X-ray beam with a width of 1600 µm and a height of 300 µm, operating at an energy of 32 keV. The 3DXRD measurement protocol employed an angular step of 0.48° to capture both far-field and near-field diffraction peaks, with exposure times of 1 s per frame for far-field images and 0.1 s per frame for near-field images. Figure 2 shows the reconstructed 3D microstructure at two different time steps.

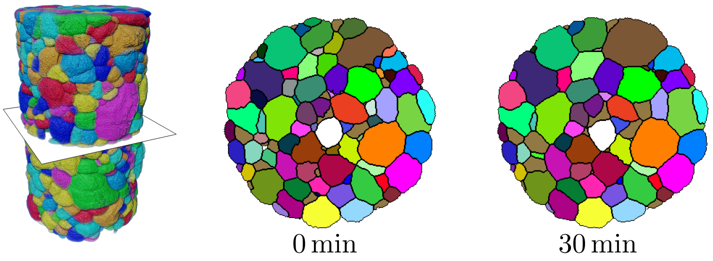

FIGURE 2. Maps of microstructure evolution in the AlMg specimen at 400 °C, recorded by 3DXRD microscopy. Only the outside surface of the cylindrical specimen is visible in the 3D rendering (left), but each such reconstruction includes the interior grain boundaries, as seen in 2D cross sections illustrating changes in interior grain shapes with increasing annealing time (middle, right). The colors of individual grains are assigned randomly; however, the same colors are mapped consistently to the same grains across all time steps.

2.2. **Extraction of grain boundaries from image data**

To enable analysis of grain boundaries captured in image data, we first extract the boundaries from the images. A grain boundary $G_{ij} \subset W$ of two adjacent grains $G_i, G_j \subset W$ for any pair

$i, j \in \{1, \ldots, n_G\}$ with $i \neq j$ is given by the image $I_{G_{ij}} \colon W \to \{0,1\}$, with

$$I_{G_{ij}}(x) = \begin{cases} 1, & \text{if } I(x) = i \text{ and } \#D_j(x) \geq 1 \text{ or } I(x) = j \text{ and } \#D_i(x) \geq 1, \\ 0, & \text{otherwise,} \end{cases} \tag{9}$$

for each $x \in W$, where $\#$ denotes cardinality and $D_k(x) = \{y \in W \colon \|x - y\| = 1 \text{ and } I(y) = k\}$ is the 6-neighborhood of the voxel $x \in W$ within grain G_k for $k \in \{1, \ldots, n_G\}$. The grain boundary G_{ij} is then given by $G_{ij} = \{x \in W \colon I_{G_{ij}}(x) = 1\}$, with $n_{G_{ij}} = \#G_{ij}$ being the number of grain boundary points belonging to this grain boundary.

3. Surface representation of grain boundaries

Image datasets of polycrystalline microstructures are usually specified in a discrete, voxel-based manner, which provides easy access to the volume of individual grains and the grain size distribution. However, voxelized representations of microstructures introduce problems in the analysis of grain boundaries and their descriptors, such as surface area or mean curvature. To address this, we propose a method that fits a surface to each voxelized grain boundary image using smoothing thin-plate splines [47, 48]. The process of creating such a surface representation is detailed in Section 3.1. Because a thin-plate spline is a composition of differentiable functions, once a grain boundary has been represented by a surface defined by such splines, the mean curvature can be computed at each point using standard methods from differential geometry [61, 62], as described in Section 3.2. When using this method to represent a grain boundary at consecutive time steps by two surfaces (see Section 3.3), it is possible to compute local variations in velocity and reduced mobility, as described in Section 3.4.

3.1. Surface representation using smoothing thin-plate splines

To represent a grain boundary $G_{ij} \subset W$ by a surface in $\mathbb{R}^3$, the set G_{ij} is first transformed by a rigid (translation and rotation) transformation $T : \mathbb{R}^3 \to \mathbb{R}^3$ [63, 64]. The translation aligns the centroid of the grain boundary voxel coordinates with the origin of $\mathbb{R}^3$. The rotation is determined by applying a principal component analysis (PCA) [65] to the set of translated voxel coordinates, which identifies a plane in $\mathbb{R}^3$ that best represents this set. This plane is then aligned with the (x,y)-coordinate plane of $\mathbb{R}^3$ through an appropriate rotation. As a result of this transformation, the set G_{ij} is represented by the set

$$K_{\mathrm{xy}} = \{(p_{\mathrm{x}}^{(k)}, p_{\mathrm{y}}^{(k)}) : k \in \{1, 2, \ldots, n_{G_{ij}}\}\}, \tag{10}$$

which contains the x- and y-components of the transformed grain boundary voxel coordinates, and the set $K_{\mathrm{z}} = \{p_{\mathrm{z}}^{(k)} \colon k \in \{1, 2, \ldots, n_{G_{ij}}\}\}$ which contains the corresponding z-components. These sets of transformed voxel coordinates will be utilized to represent grain boundaries by a surface $S \subset \mathbb{R}^3$ of the form

$$S = \{(p_{\mathrm{x}}, p_{\mathrm{y}}, s(p_{\mathrm{x}}, p_{\mathrm{y}})) \colon (p_{\mathrm{x}}, p_{\mathrm{y}}) \in A\} \tag{11}$$

with some surface function $s \colon \mathbb{R}^2 \to \mathbb{R}$ and a bounded domain $A \subset \mathbb{R}^2$. These types of surfaces are continuous representations of transformed grain boundaries using the function s, which maps points in A onto the z-coordinate of the surface S. In order to represent a transformed grain boundary with S, the surface function s has to be fitted by means of the sets K_{xy} and K_{z} introduced above. Note that without constraining the surface function to a bounded domain A, the surface S given in Eq. (11) would result in an infinitely large (unbounded) set. In order to construct a suitable bounded domain A, we construct an alpha shape of the set K_{xy}, which is determined using the Matlab function `alphaShape` — see [66, 67] for additional details.

The surface function $s : A \to \mathbb{R}$ is modeled by a parametric function $s_w\colon A \to \mathbb{R}$ with some parameter vector $w = (w^{(1)}, w^{(2)}, \dots, w^{(n_{G_{ij}})}) \in \mathbb{R}^{n_{G_{ij}}}$. The values of s_w are given by

$$s_w(p_{\mathrm{x}}, p_{\mathrm{y}}) = \sum_{k=1}^{n_{G_{ij}}} w^{(k)} \varphi(\|(p_{\mathrm{x}}, p_{\mathrm{y}}) - (p_{\mathrm{x}}^{(k)}, p_{\mathrm{y}}^{(k)})\|), \tag{12}$$

for each $(p_{\mathrm{x}}, p_{\mathrm{y}}) \in A$. Here, $\varphi\colon [0, \infty) \to \mathbb{R}$ is a radial basis function that is given by the thin-plate spline $\varphi(r) = r^2 \log(r)$ for each $r > 0$ and $\varphi(r) = 0$ for $r = 0$, where log denotes the natural logarithm. The advantage of employing thin-plate splines over other radial basis functions lies in their property of minimizing the bending energy among all twice-differentiable functions used for interpolation. Thus, the use of thin-plate splines results in a particularly smooth fitted surface, which is well-suited for accurately representing grain boundaries in the context of the present paper. For more details on thin plate splines, the reader is referred to Refs. [49–52, 68].

Although thin-plate splines inherently introduce a smoothing effect, omitting smoothing when generating a surface representation from voxelized image data may result in a surface that reproduces the voxelized geometry too closely. Therefore, the parameter vector w is determined by minimizing a loss function that accounts for the smoothness of the resulting surface by introducing an additional smoothing parameter $\lambda \in [0, 1]$. More precisely, a good choice $\widehat{w} \in \mathbb{R}^{n_{G_{ij}}}$ of the parameter vector w for a given value of λ is obtained from

$$\widehat{w} = \operatorname*{arg\,min}_{w \in \mathbb{R}^{n_{G_{ij}}}} \left(\lambda \frac{1}{n_{G_{ij}}} \sum_{k=1}^{n_{G_{ij}}} \|p_{\mathrm{z}}^{(k)} - s_w(p_{\mathrm{x}}^{(k)}, p_{\mathrm{y}}^{(k)})\|^2 + (1 - \lambda) L(s_w) \right), \tag{13}$$

where $L(s_w)$ controls the surface roughness, which is given by

$$L(s_w) = \int_A \left[\left(\frac{\partial^2 s_w(p_{\mathrm{x}}, p_{\mathrm{y}})}{\partial p_{\mathrm{x}}^2} \right)^2 + 2 \left(\frac{\partial^2 s_w(p_{\mathrm{x}}, p_{\mathrm{y}})}{\partial p_{\mathrm{x}} \partial p_{\mathrm{y}}} \right)^2 + \left(\frac{\partial^2 s_w(p_{\mathrm{x}}, p_{\mathrm{y}})}{\partial p_{\mathrm{y}}^2} \right)^2 \right] \mathrm{d}(p_{\mathrm{x}}, p_{\mathrm{y}}).$$

Here, $\partial^2 s_w(\cdot)/\partial^2(\cdot)$ denotes the second-order partial derivatives of s_w with respect to the variables p_{x} and p_{y}, respectively. For a given value of λ, the optimal parameter vector $\widehat{w}$ is computed using the Matlab function `tpaps` [69].

To obtain a good choice $\widehat{\lambda} \in [0, 1]$ for the smoothing parameter λ, a heuristic approach is proposed. This approach is based on fitting an ellipsoid and a surface S by means of Eq. (11) with surface function s_w to the transformed set of grain boundary voxels. Note that part of the boundary of the fitted ellipsoid also corresponds to a surface. The parameter $\widehat{\lambda}$ is then obtained by comparing these two surfaces with respect to their local mean curvature (as described in Section 3.2) — i.e., by minimizing the mean difference between the local mean curvature of these two surfaces. This results in a sufficiently smooth surface that nevertheless preserves the global shape of the voxelized grain boundary obtained from the image data. Further details regarding the computation of $\widehat{\lambda}$ are given in Appendix A.

3.2. Computation of normal vector field and local mean curvature

The surface representation S of a grain boundary given in Eq. (11) enables computation of the normal vector field $N_S\colon S \to \mathbb{R}^3$, as well as the local mean curvature $H_S : S \to [0, \infty)$, with respect to N_S for each point of S. Note that, in the context of grain boundary migration, it is assumed that a grain boundary migrates toward its center of curvature [46, 70] — i.e., the local mean curvature is defined to take on only positive values, and its normal vector field points toward its center of curvature [71]. In the following, we describe how these quantities can be computed from the surface function s, which is then replaced by the parametric approximation s_w given in Eq. (12); see also Refs. [62, 72–74].

For this purpose, first, the upward-pointing normal vector field $\widetilde{N}_S\colon S \to \mathbb{R}^3$, which is characterized by its positive third component, and the local mean curvature $\widetilde{H}_S\colon S \to \mathbb{R}$ are computed, where

$$\widetilde{N}_S(p_\mathrm{x}, p_\mathrm{y}, p_\mathrm{z}) = \big(-\frac{\partial s(p_\mathrm{x}, p_\mathrm{y})}{\partial p_\mathrm{x}}, -\frac{\partial s(p_\mathrm{x}, p_\mathrm{y})}{\partial p_\mathrm{y}}, 1\big) \Big/ \| \big(-\frac{\partial s(p_\mathrm{x}, p_\mathrm{y})}{\partial p_\mathrm{x}}, -\frac{\partial s(p_\mathrm{x}, p_\mathrm{y})}{\partial p_\mathrm{y}}, 1\big) \|$$

and

$$\widetilde{H}_S(p_\mathrm{x}, p_\mathrm{y}, p_\mathrm{z}) = \frac{\Big(1+\frac{\partial s(p_\mathrm{x},p_\mathrm{y})}{\partial p_\mathrm{x}}\Big)^2 \frac{\partial^2 s(p_\mathrm{x},p_\mathrm{y})}{\partial^2 p_\mathrm{y}} - 2\frac{\partial s(p_\mathrm{x},p_\mathrm{y})}{\partial p_\mathrm{x}} \frac{\partial s(p_\mathrm{x},p_\mathrm{y})}{\partial p_\mathrm{y}} \frac{\partial^2 s(p_\mathrm{x},p_\mathrm{y})}{\partial p_\mathrm{x} \partial p_\mathrm{y}} + \Big(1+\frac{\partial s(p_\mathrm{x},p_\mathrm{y})}{\partial p_\mathrm{y}}\Big)^2 \frac{\partial^2 s(p_\mathrm{x},p_\mathrm{y})}{\partial^2 p_\mathrm{x}}}{2\Big(1+\Big(\frac{\partial s(p_\mathrm{x},p_\mathrm{y})}{\partial p_\mathrm{x}}\Big)^2 + \Big(\frac{\partial s(p_\mathrm{x},p_\mathrm{y})}{\partial p_\mathrm{y}}\Big)^2\Big)^{\frac{3}{2}}} \tag{14}$$

for each $(p_\mathrm{x}, p_\mathrm{y}, p_\mathrm{z}) \in S$. Second, the local mean curvature $H_S(p_\mathrm{x}, p_\mathrm{y}, p_\mathrm{z})$ at $(p_\mathrm{x}, p_\mathrm{y}, p_\mathrm{z}) \in S$ is computed by

$$H_S(p_\mathrm{x}, p_\mathrm{y}, p_\mathrm{z}) = |\widetilde{H}_S(p_\mathrm{x}, p_\mathrm{y}, p_\mathrm{z})|, \tag{15}$$

and the normal vector $N_S(p_\mathrm{x}, p_\mathrm{y}, p_\mathrm{z})$ at $(p_\mathrm{x}, p_\mathrm{y}, p_\mathrm{z}) \in S$ is given by

$$N_S(p_\mathrm{x}, p_\mathrm{y}, p_\mathrm{z}) = \mathrm{sgn}(\widetilde{H}_S(p_\mathrm{x}, p_\mathrm{y}, p_\mathrm{z}))\widetilde{N}_S(p_\mathrm{x}, p_\mathrm{y}, p_\mathrm{z}), \tag{16}$$

where $\mathrm{sgn}\colon \mathbb{R} \to \{-1, 0, 1\}$ denotes the sign function with

$$\mathrm{sgn}(x) = \begin{cases} 1, & \text{if } x > 0, \\ 0, & \text{if } x = 0, \\ -1, & \text{if } x < 0. \end{cases}$$

3.3. **Time-resolved surface representation of grain boundaries**

To examine a given grain boundary at two successive time steps t and $t + \Delta t$, for some $t \geq 0$ and $\Delta t > 0$, the grain boundary is first extracted from the image data at the respective time steps, as described in Section 2.2. The grain boundaries between the ith and jth grain at t and $t + \Delta t$ are denoted by $G_{ij,t}$ and $G_{ij,t+\Delta t}$, respectively. The surface representations of $G_{ij,t}$ and $G_{ij,t+\Delta t}$ are constructed by means of Eq. (11) and denoted by S_t and $S_{t+\Delta t}$, respectively. However, to obtain the surface $S_{t+\Delta t}$, the same rigid transformation that was performed on $G_{ij,t}$ for the construction of S_t is also applied to $G_{ij,t+\Delta t}$. This ensures that the relative positions of the grain boundaries at two consecutive time steps remain the same even after the rigid transformation. The two surfaces S_t and $S_{t+\Delta t}$ are given by

$$S_t = \{(p_\mathrm{x}, p_\mathrm{y}, s_t(p_\mathrm{x}, p_\mathrm{y})) \in \mathbb{R}^3\colon (p_\mathrm{x}, p_\mathrm{y}) \in A_t\} \tag{17}$$

and

$$S_{t+\Delta t} = \{(p_\mathrm{x}, p_\mathrm{y}, s_{t+\Delta t}(p_\mathrm{x}, p_\mathrm{y})) \in \mathbb{R}^3\colon (p_\mathrm{x}, p_\mathrm{y}) \in A_{t+\Delta t}\}, \tag{18}$$

where the corresponding surface functions are denoted by $s_t\colon A_t \to \mathbb{R}$ and $s_{t+\Delta t}\colon A_{t+\Delta t} \to \mathbb{R}$, respectively. The domains A_t and $A_{t+\Delta t}$ are constructed as alpha shapes as described in Section 3.1. An illustration of the time-resolved surface representation of grain boundaries is provided in Figure 3(a), where a grain boundary at times t and $t + \Delta t$ is modeled by a surface that migrates upward in the vertical direction and simultaneously shrinks in area.

3.4. **Local velocity and reduced mobility of grain boundaries**

The time-resolved surface representations of a grain boundary defined above enable us to compute the velocity of grain boundaries locally — that is, for individual points on the grain boundaries. In the present section, we explain how the migration of points on a grain boundary is tracked between two consecutive time steps and how the pointwise velocity and reduced mobility are computed.

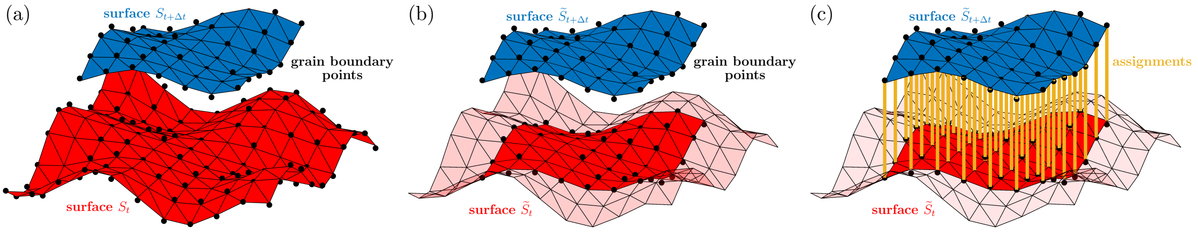

FIGURE 3. Surface representation and pointwise tracking of grain boundaries over time. (a) Surface representations S_t (red surface) and $S_{t+\Delta t}$ (blue surface), which are constructed using the sets $G_{ij,t}$ and $G_{ij,t+\Delta t}$ of grain boundary voxels (black dots) extracted from 3D image data and rigidly transformed, as described in Section 3.3. (b) Restricted surface representations $\widetilde{S}_t$ and $\widetilde{S}_{t+\Delta t}$ for assessing grain boundary migration in the overlapping region, and (c) point-by-point assignment, as described in Section 3.4.1.

3.4.1. ***Pointwise tracking of grain boundaries.*** The procedure of tracking the migration of grain boundaries is based on the time-resolved surface representations described in Section 3.3. In general, each point on a grain boundary is assumed to migrate with time in the direction of its center of curvature, which corresponds to its local normal direction. However, since the precise trajectory of a point on S_t within the time interval $[t, t + \Delta t]$ is unknown (because image measurements can only be performed for non-infinitesimal time steps, and possible inaccuracies occur when estimating the normal vector from voxelized image data), a different approach is proposed. This method is based on constructing a pointwise correspondence between the surface representations S_t and $S_{t+\Delta t}$. Once the displacement of each grain boundary point has been established, it is straightforward to compute the local velocity values.

Another challenge arises from triple junctions (curves of intersection of grain boundaries), the migration of which can add or remove area from a given grain boundary independently of the change in area entailed by migration of the grain boundary itself. To mitigate this issue, only the migration of points belonging to the intersection $A_t \cap A_{t+\Delta t}$ of the surface function domains A_t and $A_{t+\Delta t}$ is considered. This means that a point-by-point assignment is applied only to the restricted surface representations

$$\widetilde{S}_t = \{(p_{\mathrm{x}}, p_{\mathrm{y}}, s_t(p_{\mathrm{x}}, p_{\mathrm{y}})) \in \mathbb{R}^3 \colon (p_{\mathrm{x}}, p_{\mathrm{y}}) \in A_t \cap A_{t+\Delta t}\} \tag{19}$$

and

$$\widetilde{S}_{t+\Delta t} = \{(p_{\mathrm{x}}, p_{\mathrm{y}}, s_{t+\Delta t}(p_{\mathrm{x}}, p_{\mathrm{y}})) \in \mathbb{R}^3 \colon (p_{\mathrm{x}}, p_{\mathrm{y}}) \in A_t \cap A_{t+\Delta t}\},$$

as illustrated in Figure 3(b).

The pointwise correspondence is constructed in such a manner that multiple assignments of points are excluded, and the sum of Euclidean distances between all assignments is minimized. In the literature, this is known as an assignment problem [75,76]; the point-by-point assignment can be obtained from the Matlab function `matchpairs`, which employs the algorithm proposed in Ref. [77]. More precisely, the pointwise assignment is applied to finite (discretized) subsets $\widetilde{S}_{\mathrm{d},t}$ and $\widetilde{S}_{\mathrm{d},t+\Delta t}$ of $\widetilde{S}_t$ and $\widetilde{S}_{t+\Delta t}$, respectively; see Figure 3(c). These discretized versions are given by

$$\widetilde{S}_{\mathrm{d},t} = \{(p_{\mathrm{x}}, p_{\mathrm{y}}, s_t(p_{\mathrm{x}}, p_{\mathrm{y}})) \in \mathbb{R}^3 \colon (p_{\mathrm{x}}, p_{\mathrm{y}}) \in K_{\mathrm{xy},t} \cap A_t \cap A_{t+\Delta t}\} \tag{20}$$

and

$$\widetilde{S}_{\mathrm{d},t+\Delta t} = \{(p_{\mathrm{x}}, p_{\mathrm{y}}, s_{t+\Delta t}(p_{\mathrm{x}}, p_{\mathrm{y}})) \in \mathbb{R}^3 \colon (p_{\mathrm{x}}, p_{\mathrm{y}}) \in K_{\mathrm{xy},t+\Delta t} \cap A_t \cap A_{t+\Delta t}\},$$

where $K_{\mathrm{xy},t}$ and $K_{\mathrm{xy},t+\Delta t}$ are time-dependent versions of the sets of transformed grain boundary voxel coordinates introduced in Eq. (10). After performing a point-by-point assignment on the discrete sets $\widetilde{S}_t$ and $\widetilde{S}_{t+\Delta t}$, we obtain an assignment of each $p_t \in \widetilde{S}_{\mathrm{d},t}$ to a point $p_{t+\Delta t} \in \widetilde{S}_{\mathrm{d},t+\Delta t}$.

It should be noted that, upon discretizing the corresponding (continuous) surface representation — which is an essential step for determining point-by-point assignments — the meaning of quantities such as the local mean curvature or the normal vector (see Section 3.2) for points on these discretized surfaces becomes unclear. To address this issue, the local mean curvature and normal vector of points on a discretized surface representation $\widetilde{S}_{\mathrm{d},t}$ are instead associated with the curvature and normal vector of these points on the corresponding continuous surface representation $\widetilde{S}_t$. More precisely, for a point $p_t \in \widetilde{S}_{\mathrm{d},t}$, the curvature $H_S(p_t)$ and the normal vector $N_S(p_t)$ are determined according to Eqs. (15) and (16), where $S = \widetilde{S}_t$. In the following, we use the notation $H_S(p_t)$ for the local mean curvature of a point $p_t \in \widetilde{S}_{\mathrm{d},t}$, without specifying that $S = \widetilde{S}_t$.

3.4.2. ***Local velocity of grain boundaries.*** After the grain boundary points have been tracked over time, the time-dependent displacement of these points can be determined. More precisely, for each $p_t \in \widetilde{S}_{\mathrm{d},t}$ assigned to a point $p_{t+\Delta t} \in \widetilde{S}_{\mathrm{d},t+\Delta t}$, its displacement vector $D(p_t) \in \mathbb{R}^3$ is given by

$$D(p_t) = p_{t+\Delta t} - p_t, \tag{21}$$

where $d(p_t) = \|D(p_t)\| \geq 0$ denotes the displacement of p_t.

If each point p_t migrates solely in the direction of the center of curvature at that point, the normal vector $N_S(p_t)$ from Eq. (16) and the displacement vector $D(p_t)$ would be equal up to a scaling factor — i.e., the equation

$$D(p) = hN_S(p),$$

would hold for some $h > 0$. To assess the validity of this assumption, the proposed model leverages the ability to distinguish between the component of displacement in the direction of the surface normal (*normal* direction) and the component lying within the tangent plane (*in-plane* direction), which is orthogonal to the normal vector. The normal displacement vector $D_{\mathrm{n}}(p_t)$ of p_t is given by

$$D_{\mathrm{n}}(p_t) = \frac{(D(p_t), N_S(p_t))}{\|N_S(p_t)\|} N_S(p_t), \tag{22}$$

where $(\cdot,\cdot)$ denotes the dot product. The displacement of p_t in the normal direction is then given by $d_{\mathrm{n}}(p_t) = \|D_{\mathrm{n}}(p_t)\| \geq 0$. Furthermore, the displacement vector in the in-plane direction is given by $D_{\perp}(p_t) = D(p_t) - D_{\mathrm{n}}(p_t)$. To analyze the extent to which the direction of movement of p_t deviates from the normal direction, we compute the displacement angle $\alpha(p_t) \in [0, 2\pi)$ between $D(p_t)$ and $D_{\mathrm{n}}(p_t)$ for each $p_t \in \widetilde{S}_{\mathrm{d},t}$ (cf. Figure 4). A grain boundary point p_t migrates exactly toward its center of curvature if $D(p_t) = D_{\mathrm{n}}(p_t)$, which is equivalent to $\alpha(p_t) = 0$.

With the displacement vector $D(p_t)$ defined in Eq. (21), the local velocity vector $V(p_t)$ at $p_t \in \widetilde{S}_{\mathrm{d},t}$ is given by

$$V(p_t) = \frac{D(p_t)}{\Delta t}, \tag{23}$$

with local velocity $v(p_t) = \|V(p_t)\|$. Similarly, the local velocity vectors $V_{\mathrm{n}}(p_t)$ and $V_{\perp}(p_t)$ in the normal and in-plane directions, respectively, are given by $V_{\mathrm{n}}(p_t) = D_{\mathrm{n}}(p_t)/\Delta t$ and $V_{\perp}(p_t) = D_{\perp}(p_t)/\Delta t$. The local velocities in normal and in-plane directions are then given by $v_{\mathrm{n}}(p_t) = \|V_{\mathrm{n}}(p_t)\|$ and $v_{\perp}(p_t) = \|V_{\perp}(p_t)\|$.

(a) (b)

FIGURE 4. 2D illustration of the procedure for computing displacement vectors of grain boundary points. (a) Pointwise correspondence of points $p_t^{(k)} \in \widetilde{S}_{\mathrm{d},t}$ with points $p_{t+\Delta t}^{(k)} \in \widetilde{S}_{\mathrm{d},t+\Delta t}$, assigned as described in Section 3.4.1. (b) The displacement between two assigned points p_t and $p_{t+\Delta t}$ is computed separately in normal and in-plane directions, expressed by the displacement vectors $D_{\mathrm{n}}(p_t)$ and $D_\perp(p_t)$, respectively, along with the displacement angle $\alpha(p_t)$ between $D(p_t)$ and $D_{\mathrm{n}}(p_t)$.

3.4.3. ***Local reduced mobility of grain boundaries.*** It should be noted that the velocity of each grain boundary cannot be observed directly at each time step t, but only inferred as an aggregated quantity from two consecutive time steps t and $t+\Delta t$. Moreover, the evolution of the microstructure between these time steps depends on the mean curvature at each time. Therefore, the temporal change of local mean curvature must be incorporated into the computation of local reduced mobility. More precisely, for each $p_t \in \widetilde{S}_{\mathrm{d},t}$ assigned to $p_{t+\Delta t} \in \widetilde{S}_{\mathrm{d},t+\Delta t}$, the local mean curvature $H_S(p_t)$ for the surface $\widetilde{S}_{\mathrm{d},t}$ and the local mean curvature $H_S(p_{t+\Delta t})$ for the surface $\widetilde{S}_{\mathrm{d},t+\Delta t}$ are computed to obtain the change in mean curvature $\overline{H}_S$, which is given by

$$\overline{H}_S(p_t) = \frac{1}{\frac{1}{2}\left(\frac{1}{H_S(p_t)} + \frac{1}{H_S(p_{t+\Delta t})}\right)}. \tag{24}$$

Then, the local reduced mobility $\widetilde{M}(p_t) \geq 0$ of the point $p_t \in \widetilde{S}_{\mathrm{d},t}$, which is assigned to $p_{t+\Delta t} \in \widetilde{S}_{\mathrm{d},t+\Delta t}$, is computed via

$$\widetilde{M}(p_t) = \frac{v(p_t)}{\overline{H}_S(p_t)}, \tag{25}$$

according to Eq. (2). Furthermore, the local reduced mobility at $p_t \in \widetilde{S}_{\mathrm{d},t}$ in the normal direction is given by $\widetilde{M}_{\mathrm{n}}(p_t) = v_{\mathrm{n}}(p_t)/\overline{H}_S(p_t)$, and in the in-plane direction by $\widetilde{M}_\perp(p_t) = v_\perp(p_t)/\overline{H}_S(p_t)$.

4. Model validation

The primary objectives of this study are to develop methods for computing local mean curvatures and local velocities along individual grain boundaries, with the goal of estimating their local reduced mobility, where a central challenge lies in deriving these quantities from the voxel-based representations of grain boundaries extracted from 3D image data. These considerations give rise to two fundamental questions: (1) Can the proposed model accurately reconstruct smooth surface representations of grain boundaries from voxelized data? (2) If the model provides an appropriate continuous representation of a grain boundary, is it then possible to track the migration of individual grain boundary points reliably over time? These questions are systematically examined below to evaluate the general applicability of the proposed approach. For this purpose, the method is applied to the synthetic datasets introduced in Sections 2.1.1 and 2.1.2.

It is important to note that, for the synthetic datasets, ground truth values of various geometric and kinematic descriptors are available. These ground truth values are used to assess the accuracy of the proposed surface representation method and the resulting kinematic descriptors. In the case of the multiplicatively weighted Laguerre tessellation, each grain boundary of the tessellation is analytically defined by a quadratic surface, which allows for a direct comparison between the analytic grain boundary and the fitted surface representation. In particular, for this dataset, the local mean curvature at each grain boundary point is known and treated as the ground truth, enabling the evaluation of question (1). For the Reuleaux tetrahedron dataset, multiple iterations of a 3D phase field algorithm [10] were carried out starting from the initial Reuleaux tetrahedron. A specific value of the grain boundary reduced mobility is input to the phase field algorithm and incorporated into the equation of motion; this value is taken to be the ground truth for the reduced mobility. Consequently, this dataset enables the investigation of question (2).

It should be pointed out that discrepancies between computed geometric and kinematic values and their ground truths can occur due to various reasons, such as approximation or representation errors. Moreover, in the context of this paper, it is difficult to carry out a direct comparison between, on the one hand, geometric and kinematic descriptors obtained from the surface representations and, on the other hand, the corresponding ground truth values. This difficulty arises from the fact that the ground truth data are derived from continuous analytic representations of the tessellation and of the Reuleaux tetrahedron, whereas the proposed method operates on voxelized versions of these datasets, which inherently introduces discretization errors. For instance, in the tessellation-based datasets, the input data for determining the surface representations are not the analytic grain boundaries themselves, but rather their voxelized representations. The latter type of representation already introduces errors, even before the proposed surface representation method has been deployed. Similarly, for the Reuleaux tetrahedron, the output of the 3D phase field algorithm is also discretized before applying the surface fitting procedure to its grain boundaries. Despite these inherent sources of error, the two synthetic datasets provide a reasonably good basis for validating the proposed methodology.

4.1. **Smooth surface representation of tessellation grain boundaries**

To assess the capability of the proposed model to represent grain boundaries extracted from image data, it is first applied to a multiplicatively weighted Laguerre tessellation, which includes a wide variety of differently shaped grain boundaries (see Section 2.1.1). In previous studies, this tessellation model has been fitted to experimental data [40, 41, 43], and it has been found to exhibit grain boundary structures comparable to those observed in real microstructures. A quantitative assessment of the model's accuracy in reconstructing both the surface geometry and, in particular, the local mean curvature is obtained by evaluating the pointwise accuracy, which is outlined in Section 4.1.1. Because in this work the multiplicatively weighted Laguerre tessellation is specified on a voxel grid, all variables considered in this section are given in voxels (voxel unit).

4.1.1. ***Pointwise accuracy.*** Instead of S, the notation S_{ij} is used here to denote the surface representation of grain boundary C_{ij} between two adjacent grains i and j of the multiplicatively weighted Laguerre tessellation, for any $i, j \in \{1, 2, \dots, n_{\mathcal{T}}\}$ with $i \neq j$ — see Eq. (5). The discretized representation of C_{ij} is denoted by G_{ij} and obtained from image data as described in Section 2.2. To enable a direct comparison between C_{ij} and S_{ij} — where S_{ij} is fitted with respect to G_{ij} and represents C_{ij} in a rigidly transformed coordinate frame (see Section 3.1) — the surface S_{ij} is first discretized. We consider the discretized version $S_{\mathrm{d},ij} \subset S_{ij}$ given by

$S_{\mathrm{d},ij} = \{(p_\mathrm{x}, p_\mathrm{y}, s(p_\mathrm{x}, p_\mathrm{y}))\colon (p_\mathrm{x}, p_\mathrm{y}) \in K_{\mathrm{xy,ij}}\}$, where $K_{\mathrm{xy,ij}}$ is given by Eq. (10) for the set G_{ij} and s denotes the surface function, which is fitted as described in Section 3.1. Then, the discretized surface representation $S_{\mathrm{d},ij}$ is transformed with the corresponding inverse rigid transformation $T_{ij}^{-1}\colon \mathbb{R}^3 \to \mathbb{R}^3$ to obtain the surface $S'_{\mathrm{d},ij} = T_{ij}^{-1}(S_{\mathrm{d},ij})$. Subsequently, each point $p' \in S'_{\mathrm{d},ij}$ is assigned to a point p on C_{ij} that has the smallest Euclidean distance to p'. More formally, the mapping $O\colon S'_{\mathrm{d},ij} \to C_{ij}$ is considered, which is given by

$$O(p') = \underset{p \in C_{ij}}{\arg\min} \|p' - p\| \tag{26}$$

for each $p' \in S'_{\mathrm{d},ij}$. Numerically, the minimization problem stated in Eq. (26) is solved using the Matlab function `fmincon`.

Accuracy of surface representation. First, the function $\delta : S'_{\mathrm{d},ij} \to [0, \infty)$, given by

$$\delta(p') = \|O(p') - p'\| \tag{27}$$

for each $p' \in S'_{\mathrm{d},ij}$, is used to evaluate the model fit. This function enables us to assess how well the back-transformed surface $S'_{\mathrm{d},ij}$ aligns pointwise with the underlying grain boundary G_{ij}. Small values of $\delta(p')$ indicate that the surface representation accurately mimics the corresponding analytic grain boundary at $p' \in S'_{\mathrm{d},ij}$.

Local mean curvature accuracy. Second, the model is evaluated in terms of its accuracy in estimating local mean curvature values. Recall that the grain boundary between two grains can be represented by a quadratic surface — see Eq. (5) — and the local mean curvature can be computed as described in Ref. [41]. Therefore, we consider the function $\widetilde{C}_{ij}\colon \mathbb{R}^3 \to \mathbb{R}$ given by

$$\widetilde{C}_{ij}(x) = \|x - g_i\|^2 m_i - a_i - \|x - g_j\|^2 m_j + a_j, \tag{28}$$

for each $x \in \mathbb{R}^3$, with seed points g_i and g_j, multiplicative weights m_i and m_j, and additive weights a_i and a_j of grains G_i and G_j (cf. Section 2.1.1). Note that $\widetilde{C}_{ij}(x) = 0$ for each $x \in C_{ij}$. For the function $\widetilde{C}_{ij}$ introduced in Eq. (28), the gradient is denoted by $\nabla_{\widetilde{C}_{ij}}\colon \mathbb{R}^3 \to \mathbb{R}^3$, the Hessian matrix by $\mathrm{Hess}_{\widetilde{C}_{ij}}\colon \mathbb{R}^3 \to \mathbb{R}^{3\times 3}$ and the trace by $\mathrm{tr}\colon \mathbb{R}^{3\times 3} \to \mathbb{R}$ — see Ref. [74]. Note that the partial derivatives of $\widetilde{C}_{ij}$ are obtained by utilizing the implicit function theorem [78]. Then, the local mean curvature $H^*\colon C_{ij} \to \mathbb{R}$ is given by

$$H^*(x) = \frac{\nabla_{\widetilde{C}_{ij}}(x)\mathrm{Hess}_{\widetilde{C}_{ij}}(x)\nabla_{\widetilde{C}_{ij}}(x)^\top - \|\nabla_{\widetilde{C}_{ij}}(x)\|^2 \mathrm{tr}(\mathrm{Hess}_{\widetilde{C}_{ij}}(x))}{2\|\nabla_{\widetilde{C}_{ij}}(x)\|^3}, \tag{29}$$

for each $x \in C_{ij}$ — see Eq. (16) in Ref. [40] — where $\nabla_{\widetilde{C}_{ij}}(x)^\top$ denotes the transposed matrix of $\nabla_{\widetilde{C}_{ij}}(x)$. In the special case of a multiplicatively weighted Laguerre tessellation, Eq. (29) simplifies to $H^*(x) = -2(m_i - m_j)/\|\nabla_{\widetilde{C}_{ij}}(x)\|$ for each $x \in C_{ij}$.

For each $p' \in S'_{\mathrm{d},ij}$, we use the relative error $\varepsilon_{\mathrm{rel}}(p')$ between the local mean curvature $H_S(p')$ and the corresponding ground truth value $H^*(O(p'))$ to evaluate the accuracy in estimating mean curvature values. More precisely, the mapping $\varepsilon_{\mathrm{rel}}\colon S'_{\mathrm{d},ij} \to [0, \infty)$ of $p' \in S'_{\mathrm{d},ij}$ is considered, where

$$\varepsilon_{\mathrm{rel}}(p') = \left| \frac{H^*(O(p')) - H_S(p')}{H^*(O(p'))} \right|. \tag{30}$$

A small value of $\varepsilon_{\mathrm{rel}}(p')$ indicates that the local mean curvature $H_S(p')$ is close to its ground truth value $H^*(O(p'))$.

Accuracy of surface representation near triple junctions. The surface representation of grain boundaries near triple junctions is expected to be less accurate, owing to the reduced number of points available for surface fitting. Therefore, when evaluating the accuracy of the proposed method, the Euclidean distance of grain boundary points from triple junctions is additionally taken into account. More precisely, the set $J_{ij} \subset W$ of voxels corresponding to all triple junctions associated with grain boundary G_{ij} is given by

$$J_{ij} = \bigcup_{k \in \{1,2,\ldots,n_{\mathcal{T}}\} \setminus \{i,j\}} G_{ij} \cap G_{ik}. \tag{31}$$

Then, the influence of the distance of the grain boundary points to triple junctions can be evaluated by analyzing the accuracy with respect to the set $S'_{\mathrm{d},ij,d_{\min}} \subset S'_{\mathrm{d},ij}$, instead of $S'_{\mathrm{d},ij}$, where

$$S'_{\mathrm{d},ij,d_{\min}} = \{p \in S'_{\mathrm{d},ij} \colon \min_{x \in J_{ij}} \|p - x\| \geq d_{\min}\} \tag{32}$$

for some adjustable minimum distance $d_{\min} \geq 0$. In this case, the evaluation of model accuracy is restricted to points that are located at least a distance $d_{\min}$ from the triple junctions.

4.1.2. ***Fitting results.*** We now evaluate the accuracy of the surface representation model introduced in Section 3 using the functions δ and $\varepsilon_{\mathrm{rel}}$ given by Eqs. (27) and (30), respectively, focusing particularly on the effect of excluding points within $d_{\min}$ of a triple junction. Figure 5 presents box plots for the values of δ and $\varepsilon_{\mathrm{rel}}$ for various specifications of the parameter $d_{\min}$. In addition, the median and mean values of each box plot are indicated by brown and orange lines, respectively. Note that, as the value of $d_{\min}$ increases, it becomes increasingly likely for all points on smaller grain boundaries to be excluded from the accuracy analysis, thus reducing the overall number of grain boundaries included in the evaluation. The blue curve in Figure 5(b) shows the number of grain boundaries considered by the analysis at each $d_{\min}$ value.

Figure 5(a) indicates that most δ-values lie well below 0.5, indicating that the pointwise Euclidean distance between the reconstructed surface and the corresponding grain boundary of the tessellation is less than half the length of a voxel. This suggests that the surface representation model introduced in Section 3 provides a close approximation to the analytic grain boundaries of the multiplicatively weighted Laguerre tessellation. Moreover, Figure 5(a) shows that the mean and median values of δ decrease as $d_{\min}$ increases. This behavior is to be expected, since, with an increasing value of $d_{\min}$, more and more points near triple junctions are excluded from the accuracy analysis, for which the surface representation is less accurate due to the reduced number of points available for surface fitting.

The same behavior can be observed when estimating the local mean curvature, as visualized in Figure 5(b). With increasing $d_{\min}$, the values of $\varepsilon_{\mathrm{rel}}$ decrease, where this trend is even more pronounced than for δ. Furthermore, Figure 5(b) shows that the values of $\varepsilon_{\mathrm{rel}}$ are generally low for the majority of grain boundary points, as indicated by the small median value. Larger values of $\varepsilon_{\mathrm{rel}}$ may be attributed to the sensitivity of local mean-curvature computations to the second-order derivatives in Eq. (14). Consequently, even minor deviations between the fitted surface and the corresponding analytic grain boundary can lead to substantial relative errors in the estimated local mean curvature value. However, for $d_{\min} = 4$, the values of $\varepsilon_{\mathrm{rel}}$ become sufficiently small, while only a few grain boundaries are excluded by the $d_{\min}$ criterion, as evidenced by the blue curve in Figure 5(b). When analyzing a voxelized ground boundary using our method, a practical rule of thumb would be to consider only those boundary points that lie at least 4 voxels away from the triple junctions.

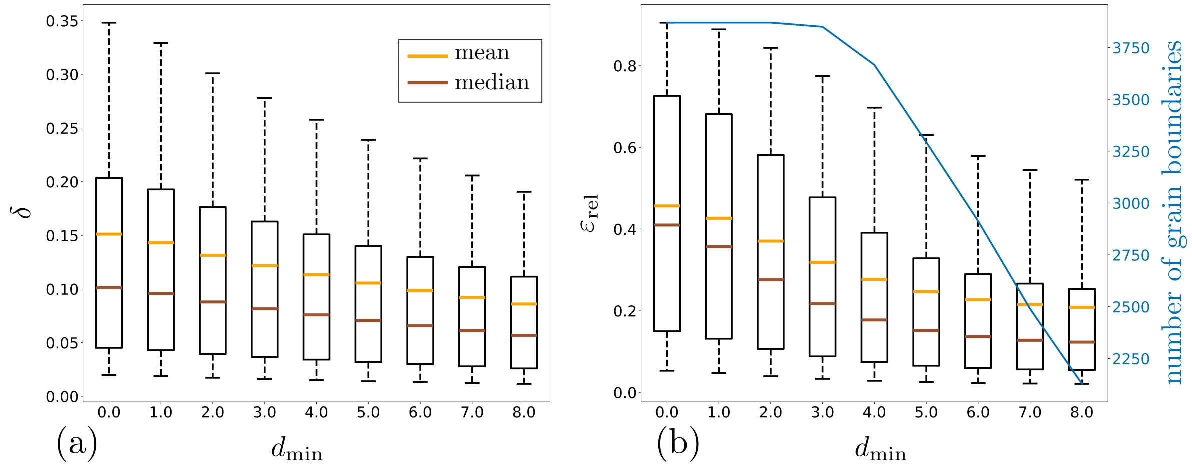

FIGURE 5. Box plots visualizing (a) values of δ for evaluating the accuracy of surface representations (Eq. (27)) and (b) values of the relative error $\varepsilon_{\mathrm{rel}}$ between local mean curvature values and the corresponding ground truth values (Eq. (30)) for all grain boundary points $p' \in S'_{\mathrm{d},ij,d_{\min}}$, excluding all points with distance less than $d_{\min}$ from triple junctions. In (b), the number of grain boundaries that remain after application of the $d_{\min}$ criterion is indicated by the blue curve. In both subfigures, the boxes are bounded by the 25th and 75th percentiles, and the whiskers extend from the 10th to the 90th percentile. Furthermore, the mean and median values are marked by orange and brown lines, respectively.

4.2. Local velocity and reduced mobility of grain boundaries: Reuleaux tetrahedron

To assess the reliability of tracking the migration of individual grain boundary points over time using the surface representation model introduced in Section 3, a Reuleaux tetrahedron (see Section 2.1.2) with a radius of $r = 80$ voxels is employed as the initial configuration for a computational simulation of grain growth according to Eq. (1). In this simulation study, 2400 iterations of a 3D phase-field algorithm [10] were performed, starting from the initial Reuleaux tetrahedron of radius $r = 80$. The results of the simulation were recorded every 800 iterations, yielding time-resolved image data at simulation steps $t \in \{0, 800, 1600, 2400\}$ with a time-step length of $\Delta t = 800$ iterations. Each point on the grain boundaries of the Reuleaux tetrahedron is assigned the same mobility and energy values (and, thus, the same reduced mobility), and the grain boundary morphology is assumed to remain that of a Reuleaux tetrahedron over time. This makes it possible to extract ground truth values for the mean curvature, grain boundary displacement and velocity at each point in time. These quantities are denoted by H_t^*, d_t^*, and v_t^*, respectively, and the reduced mobility that was input to the phase field simulation is denoted $\widetilde{M}^*$. Because the simulated microstructures are given on a voxel grid, all variables considered in this section are specified in voxels (voxel unit). Further details regarding the phase field algorithm and the determination of ground truth values may be found in Appendix B.

4.2.1. ***Surface representation approach.*** The surface representation method introduced in Section 3 is applied to the output of the phase field algorithm. Note that, at each simulation step t, the corresponding Reuleaux tetrahedron has four grain boundaries $R_{i,t}$ for $i \in \{1, 2, 3, 4\}$, with each $R_{i,t}$ represented by the discrete representation $G_{5,i,t}$ obtained from image data of the Reuleaux tetrahedron, as described in Section 2.2. For simplification, we use the notation $G_{i,t}$, instead of $G_{5,i,t}$, since only the grain boundaries of the Reuleaux tetrahedron are considered here. Each grain boundary $G_{i,t}$ is represented by the surface $\widetilde{S}_{i,t}$ given in Eq. (19), where, instead of $\widetilde{S}_t$ the notation $\widetilde{S}_{i,t}$ is used. For analyzing the migration of individual grain boundary points on each grain boundary, the discretized surface representation $\widetilde{S}_{\mathrm{d},i,t} \subset \widetilde{S}_{i,t}$ given by Eq. (20) is utilized, where, again, instead of $\widetilde{S}_{\mathrm{d},t}$ we employ the notation $\widetilde{S}_{\mathrm{d},i,t}$. To compare $\widetilde{S}_{\mathrm{d},i,t}$ to $R_{i,t}$, the surface $\widetilde{S}_{\mathrm{d},i,t}$ is transformed with the corresponding inverse rigid transformation $T_{i,t}^{-1}\colon \mathbb{R}^3 \to \mathbb{R}^3$ of the surface representation $\widetilde{S}_{i,t}$, as described in Section 3.1, resulting in the surface representation $S'_{\mathrm{d},i,t} = T_{i,t}^{-1}(\widetilde{S}_{\mathrm{d},i,t})$. For each grain boundary point $p \in \widetilde{S}_{\mathrm{d},i,t}$, the proposed method provides values for the following quantities described in Section 3.4: local mean curvature $H_S(p)$; displacement $d(p)$; displacement in the normal direction $d_\mathrm{n}(p)$; displacement angle $\alpha(p)$; velocity in normal direction $v_\mathrm{n}(p)$; reduced mobility $\widetilde{M}(p)$; and reduced mobility in the normal direction $\widetilde{M}_\mathrm{n}(p)$.

Fitting results. Figure 6 shows results obtained by the surface representation method following its application to the grain boundaries of the Reuleaux tetrahedron at $t = 0$ and $t = 800$. In Figures 6(a) and 6(c), values of $H_S(p)$ and $\alpha(p)$ are visualized for points $p \in \widetilde{S}_{\mathrm{d},i,0}$ associated with a particular grain boundary $R_{i,0}$. In Figures 6(b) and 6(d), histograms of $H_S(p)$ and $\alpha(p)$ are shown for all grain boundary points $p \in \widetilde{S}_{\mathrm{d},0,d_\mathrm{min}}$, where $\widetilde{S}_{\mathrm{d},0,d_\mathrm{min}} = \bigcup_{i\in\{1,2,3,4\}} T_{i,0}(S'_{\mathrm{d},i,0,d_\mathrm{min}})$, and $S'_{\mathrm{d},i,0,d_\mathrm{min}}$ is given by Eq. (32) for the surface representation $S'_{\mathrm{d},i,0}$. Here, points with distance less than $d_\mathrm{min} = 4$ from triple junctions are excluded, as described in Section 4.1. Note that the red lines in Figures 6(a) and 6(c) indicate grain boundary points with distance $d_\mathrm{min} = 4$ to triple junctions. In addition, in Figure 6(b), the ground truth value $H_0^* = 0.0125$, as well as the mean and median values of all $H_S(p)$ values, are plotted as green, dashed orange and dotted brown lines, respectively.

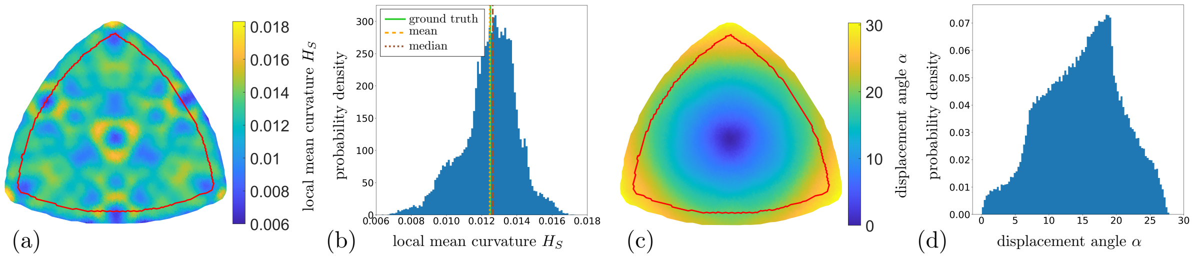

FIGURE 6. Results of the surface representation method applied to the grain boundaries of the Reuleaux tetrahedrons at steps $t = 0$ and $t = 800$. Values of (a) local mean curvature $H_S(p)$ and (c) displacement angle $\alpha(p)$ for points $p \in \widetilde{S}_{\mathrm{d},i,0}$ associated with one grain boundary $R_{i,0}$. Histogram of values of (b) $H_S(p)$ and (d) $\alpha(p)$ for all $p \in \widetilde{S}_{\mathrm{d},0,d_\mathrm{min}}$, excluding boundary points with distance less than $d_\mathrm{min} = 4$ to triple junctions, where the red line indicates all points with a distance of 4 to the triple junctions. Corresponding ground truth, mean and median values are indicated as green, dashed orange and dotted brown lines.

In addition, the surface representation method is evaluated with regard to its ability to estimate boundary displacement and local reduced mobility. In the upper row of Figure 7, from left to right, the values of $d(p)$, $d_\mathrm{n}(p)$, $\widetilde{M}(p)$ and $\widetilde{M}_\mathrm{n}(p)$ are visualized for points $p \in \widetilde{S}_{\mathrm{d},i,0}$ associated with a given grain boundary $R_{i,0}$. In the bottom row of Figure 7, histograms of the values of $d(p)$, $d_\mathrm{n}(p)$, $\widetilde{M}(p)$ and $\widetilde{M}_\mathrm{n}(p)$ are shown for all grain boundary points $p \in \widetilde{S}_{\mathrm{d},0,d_\mathrm{min}}$, excluding points with distance less than $d_\mathrm{min} = 4$ to triple junctions. Moreover, in the bottom row of Figure 7, the ground truth values $H_0^* = 0.0125$, $d_0^* = 3.08$ and $\widetilde{M}^* = 0.295$, as well as the median and mean values of $d(p)$, $d_\mathrm{n}(p)$, $\widetilde{M}(p)$ and $\widetilde{M}_\mathrm{n}(p)$, are plotted as green, dashed orange and dotted brown lines, respectively.

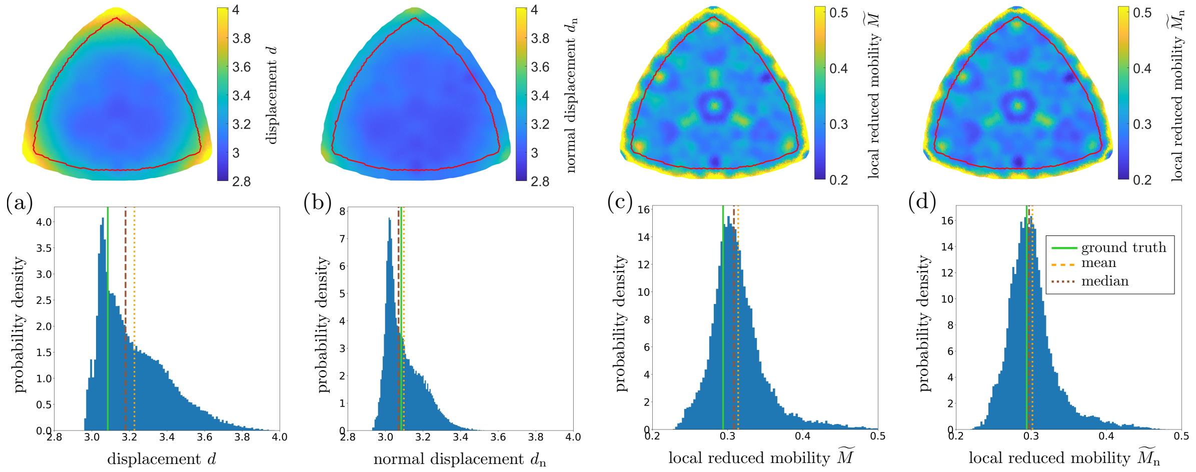

FIGURE 7. Results of the surface representation method applied to the grain boundaries of the Reuleaux tetrahedron at steps $t = 0$ and $t = 800$. Top row, left to right: Values of displacement $d(p)$, displacement $d_\mathrm{n}(p)$ in normal direction, local reduced mobility $\widetilde{M}(p)$ and local reduced mobility $\widetilde{M}_\mathrm{n}(p)$ in normal direction for points $p \in \widetilde{S}_{\mathrm{d},i,0}$ associated with a particular grain boundary $R_{i,0}$. Red lines indicate all points located a distance of 4 from the triple junctions. Bottom row, left to right: Histogram of the values of $d(p)$, $d_\mathrm{n}(p)$, $\widetilde{M}(p)$ and $\widetilde{M}_\mathrm{n}(p)$ for all $p \in \widetilde{S}_{\mathrm{d},0,d_{\min}}$, excluding boundary points with distance less than $d_{\min} = 4$ from the triple junctions. The corresponding ground truth, mean and median values are indicated as green, dashed orange and dotted brown lines, respectively.

Discussion of Reuleaux tetrahedron results. It can be observed that the proposed surface representation method closely approximates the grain boundaries of the Reuleaux tetrahedron, since the values for $H_S(p)$ closely match H_0^* for all $p \in \widetilde{S}_{\mathrm{d},0,d_{\min}}$, as long as boundary points are excluded that lie within $d_{\min} = 4$ of triple junctions — see Figure 6(b). This result is comparable to that of Section 4.1 for the multiplicatively weighted Laguerre tessellation.

Furthermore, although the values for $\alpha(p)$ deviate from zero for all $p \in \widetilde{S}_{\mathrm{d},0,d_{\min}}$ in Figure 6(d), we can conclude that each p migrates toward its center of curvature, as all $\alpha(p)$ values remain below 30°. The observed deviations from zero arise from the fact that the proposed surface representation method is applied to input data that have already been voxelized, which introduces small geometric inaccuracies. Consequently, minor reconstruction errors can lead to deviations in the estimation of the surface normal $N_S(p)$ and the mean curvature $H_S(p)$ at each point $p \in \widetilde{S}_{\mathrm{d},0,d_{\min}}$. In particular, for points with values of H_S close to zero, discrepancies can become more pronounced, and the normal vector can even undergo direction reversal.

Comparing $d(p)$ and $d_\mathrm{n}(p)$ for all $p \in \widetilde{S}_{\mathrm{d},0,d_{\min}}$ in Figures 7(a) and 7(b) (bottom row), it is evident that the values of $d_\mathrm{n}(p)$ are closer to the ground truth value d_0^* than are the $d(p)$ values. Similarly, Figures 7(c) and 7(d) (bottom row) show that the values of $\widetilde{M}_\mathrm{n}(p)$ are closer to the reference value $\widetilde{M}^*$ than are the $\widetilde{M}(p)$ values. Therefore, in the subsequent analysis of pointwise migration, only the displacement $d_\mathrm{n}(p)$, velocity $v_\mathrm{n}(p)$, and reduced mobility $\widetilde{M}_\mathrm{n}(p)$ in the normal direction are considered for each grain boundary point $p \in \widetilde{S}_{\mathrm{d},0,d_{\min}}$.

It should be noted that, in the migration analysis of the Reuleaux tetrahedron, only those grain boundary points exhibiting a minimal distance from the triple junctions of the corresponding boundary at time t were considered. These points were subsequently matched with points located on the same grain boundary at time $t + \Delta t$. However, the distances of matched points (i.e., at $t + \Delta t$) from triple junctions were not taken into account. Nevertheless, the results obtained are sufficiently accurate. In particular, for the experimental data presented in Section 5, the same surface representation method is applied to grain boundaries at time t without explicitly considering the triple junctions at time $t + \Delta t$. Incorporating triple junction information across consecutive time steps in the analysis of local grain boundary migration is a possible topic for future work.

4.2.2. ***Exchanged volume method.*** In the literature, the grain boundary velocity has been computed from the ratio of the volume exchanged between two neighboring grains during a time step Δt and the average surface area of the boundary between the same two grains, normalized by Δt [33, 46]. We refer to this approach as the exchanged volume method, and we compare it to the surface representation method introduced in the present paper. By the exchanged volume method, for a grain boundary $R_{i,t}$ of the Reuleaux tetrahedron with $i \in \{1, 2, 3, 4\}$ at simulation step $t \in \{0, 800, 1600\}$, the grain boundary velocity $v_{\mathrm{ex},i,t} \in [0, \infty)$ between t and $t + \Delta t$ is given by

$$v_{\mathrm{ex},i,t} = \frac{V_{\mathrm{ex},i,t}}{\frac{1}{2}(S_{A,i,t} + S_{A,i,t+\Delta t})\Delta t}, \tag{33}$$

where $V_{\mathrm{ex},i,t} \in [0, \infty)$ denotes the exchanged volume between t and $t + \Delta t$, which is determined from the image data by counting the voxels that are exchanged between the grains under consideration. Furthermore, $S_{A,i,t} \in [0, \infty)$ and $S_{A,i,t+\Delta t} \in [0, \infty)$ denote the surface areas of the grain boundary at consecutive time steps. In the present paper, these two surface areas are computed from 3D image data using the method proposed in Ref. [79]. It should be noted that the exchanged volume method yields a single velocity value $v_{\mathrm{ex},i,t}$ for a given grain boundary, rather than the local velocities of points on the boundary. Since all grain boundaries of the Reuleaux tetrahedron possess identical morphology and, by construction, migrate at the same velocity, it is reasonable to consider their mean velocity given by $\overline{v}_{\mathrm{ex},t} = \frac{1}{4}\sum_{i=1}^{4} v_{\mathrm{ex},i,t}$. Furthermore, the exchanged volume method provides only velocity values; it gives no information regarding the local mean curvature directly. Therefore, to compare the two methods in terms of the reduced mobility, we compute the reduced mobility $\widetilde{M}_{\mathrm{ex},t} \in [0, \infty)$ in the context of the exchanged volume method by the formula

$$\widetilde{M}_{\mathrm{ex},t} = \frac{1}{2}\overline{v}_{\mathrm{ex},t}\left(\frac{1}{\frac{1}{r_t}} + \frac{1}{\frac{1}{r_{t+\Delta t}}}\right),$$

where r_t and $r_{t+\Delta t}$ denote the radii of the Reuleaux tetrahedron at times t and $t + \Delta t$, respectively; these radii are determined by means of Eq. (43) in Appendix B.

Figure 8 presents a comparison of results obtained by the surface representation method and the exchanged volume method for the simulation steps $t \in \{0, 800, 1600\}$. In Figures 8(a) and 8(b), the values of local velocity $v_{\mathrm{n}}(p)$ and local reduced mobility $\widetilde{M}_{\mathrm{n}}(p)$ in normal direction for points $p \in \widetilde{S}_{\mathrm{d},t,d_{\min}}$ are visualized as violin and box plots, respectively. Here, the set $\widetilde{S}_{\mathrm{d},t,d_{\min}}$ is given by $\widetilde{S}_{\mathrm{d},t,d_{\min}} = \bigcup_{i\in\{1,2,3,4\}} T_t(S'_{\mathrm{d},i,t,d_{\min}})$, and $S'_{\mathrm{d},i,t,d_{\min}}$ is given by Eq. (32) for the surface representation $S'_{\mathrm{d},i,t}$, excluding points with distance less than $d_{\min} = 4$ to triple junctions. The box plots are generated as described in Section 4.1.2. In addition, the ground truth values $v_0^* = 0.0039$, $v_{800}^* = 0.0043$, $v_{1600}^* = 0.0049$ and $\widetilde{M}^* = 0.295$, as well as the median and mean values of $v_{\mathrm{n}}(p)$ and $\widetilde{M}_{\mathrm{n}}(p)$, are plotted for all $t \in \{0, 800, 1600\}$ as green dots, dotted brown and dashed orange lines, respectively. Furthermore, the values of mean velocity $\overline{v}_{\mathrm{ex},t}$ and reduced mobility $\widetilde{M}_{\mathrm{ex},t}$ obtained by the exchanged volume method are visualized as magenta squares in subfigures (a) and (b), respectively.

Both methods demonstrate comparable performance, as the values of $v_{\mathrm{n}}(p)$ and $\widetilde{M}_{\mathrm{n}}(p)$, as well as $\overline{v}_{\mathrm{ex},t}$ and $\widetilde{M}_{\mathrm{ex},t}$, closely correspond to the ground truth values v_t^* and $\widetilde{M}^*$ for all $t \in \{0, 800, 1600\}$. The distributions of $v_{\mathrm{n}}(p)$ and $\widetilde{M}_{\mathrm{n}}(p)$ are relatively symmetric around their respective mean values, which show only minor deviations from the ground truth. It should be noted that the exchanged volume approach relies on prior knowledge of the mean curvature of the Reuleaux tetrahedron to compute the reduced mobility. Although this method performs reliably when the mean curvature of an entire grain boundary is known, it yields only a single, aggregated reduced mobility value per boundary. In contrast, the surface representation method enables pointwise estimation of the reduced mobility, providing a more detailed and spatially resolved characterization of grain boundary migration behavior.

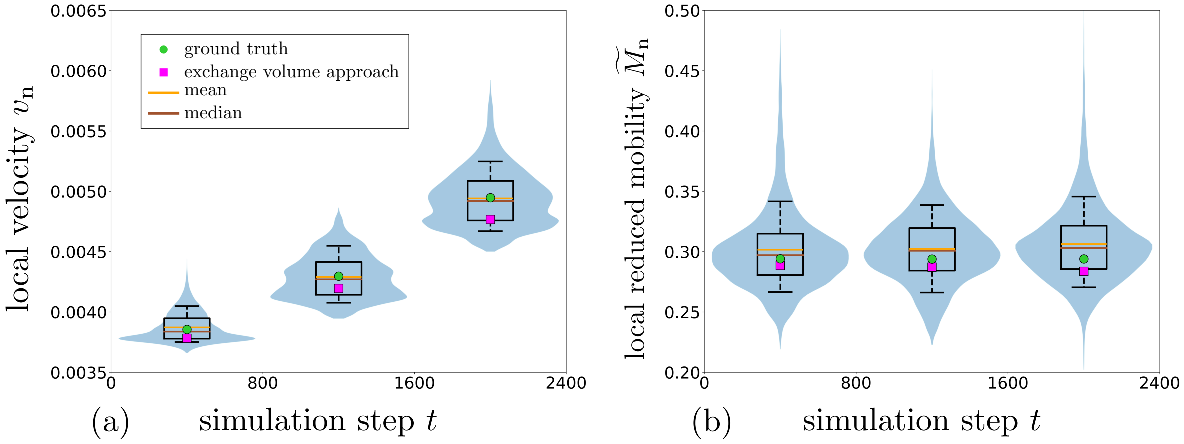

FIGURE 8. Comparison of surface representation and exchanged volume methods at steps $t \in \{0, 800, 1600\}$, showing violin plots, box plots, mean and median (orange and brown lines) of the (a) local velocity $v_\mathrm{n}(p)$ in normal direction and (b) local reduced mobility $\widetilde{M}_\mathrm{n}(p)$ in normal direction, obtained by the surface representation method for grain boundary points $p \in \widetilde{S}_{\mathrm{d},t,d_\mathrm{min}}$, excluding points with distance less than $d_\mathrm{min} = 4$ to triple junctions. Ground truth values of velocity v_t^* and reduced mobility M_t^* are indicated as green dots in (a) and (b), respectively. Furthermore, the values of mean velocity $\overline{v}_{\mathrm{ex},t}$ and mean reduced mobility $\widetilde{M}_{\mathrm{ex},t}$ that were obtained via the exchanged volume approach are indicated as magenta squares in (a) and (b), respectively. In both subfigures, the boxes are bounded by the 25th and 75th percentiles, and the whiskers extend from the 10th to the 90th percentile.

5. **Grain boundary migration in an AlMg alloy**

Employing 3D image data from two consecutive time steps, we quantify the migration of grain boundaries in the AlMg specimen described in Section 2.1.3. In the present section, the evolution of the initial microstructure that takes place during a 15-minute annealing period is analyzed using the surface representation method introduced in Section 3.1. For the time steps $t = 0\,\mathrm{min}$ and $t + \Delta t = 15\,\mathrm{min}$, we consider all grain boundaries between any two adjacent grains, with $i, j \in \{1, \dots, n_G\}$ and $i \neq j$, where $n_G > 0$ denotes the number of grains observed in the AlMg specimen at both time steps t and $t + \Delta t$. Each grain boundary is extracted from the image data following the steps described in Section 2.2, resulting in sets $G_{ij,t}$ and $G_{ij,t+\Delta t}$ of grain boundary voxels. Then, for these sets, surface representations $\widetilde{S}_{ij,t}$ and $\widetilde{S}_{ij,t+\Delta t}$ are constructed, as described in Section 3.1, where, instead of $\widetilde{S}_t$ and $\widetilde{S}_{t+\Delta t}$ the notations $\widetilde{S}_{ij,t}$ and $\widetilde{S}_{ij,t+\Delta t}$ are used to denote the surface representations of $G_{ij,t}$ and $G_{ij,t+\Delta t}$, respectively. When fitting these surface representations, the smoothing parameter λ was fixed at 0.001. This value is equal to the average smoothing parameter applied by the surface representation method to multiplicatively weighted Laguerre tessellations. In particular, this value was found to adequately preserve the geometric characteristics of each boundary while ensuring a sufficiently smooth surface representation, effectively mitigating the voxelized appearance present in the original image data input. Moreover, the decision to fix the value of λ allows the proposed method to be applied to experimental data containing a much larger number of grain boundaries without the additional computational cost of optimizing λ for each grain boundary.

To analyze the migration of individual grain boundary points on each grain boundary, we utilize the discretized surface representations $\widetilde{S}_{\mathrm{d},ij,t} \subset \widetilde{S}_{ij,t}$ and $\widetilde{S}_{\mathrm{d},ij,t+\Delta t} \subset \widetilde{S}_{ij,t+\Delta t}$ given by Eq. (20), where, instead of $\widetilde{S}_{\mathrm{d},t}$ and $\widetilde{S}_{\mathrm{d},t+\Delta t}$, the notations $\widetilde{S}_{\mathrm{d},ij,t}$ and $\widetilde{S}_{\mathrm{d},ij,t+\Delta t}$ are used. Then, each point $p_t \in \widetilde{S}_{\mathrm{d},ij,t}$ is matched with a point $p_{t+\Delta t} \in \widetilde{S}_{\mathrm{d},ij,t+\Delta t}$, as described in Section 3.4, to determine the pointwise displacement. In order to analyze the influence of local mean curvature on grain boundary migration, the local mean curvature value $H_S(p_t)$ is computed for each point $p_t \in \widetilde{S}_{\mathrm{d},ij,t}$. Furthermore, to enable a comparison between $\widetilde{S}_{\mathrm{d},ij,t}$ and $G_{ij,t}$ and, in particular, to account for the distances of points in $\widetilde{S}_{\mathrm{d},ij,t}$ from the triple junctions, the surface $\widetilde{S}_{\mathrm{d},ij,t}$ is transformed back with its corresponding inverse rigid transformation $T^{-1}_{ij,t} \colon \mathbb{R}^3 \to \mathbb{R}^3$, as described in Section 3.1, resulting in the surface representation $S'_{\mathrm{d},ij,t} = T^{-1}_{ij,t}(\widetilde{S}_{\mathrm{d},ij,t})$. For simplicity, since only a single time step is considered in this context, the notations G_{ij}, $\widetilde{S}_{\mathrm{d},ij}$, $S'_{\mathrm{d},ij}$ and T^{-1}_{ij} are used in the following instead of $G_{ij,t}$, $\widetilde{S}_{\mathrm{d},ij,t}$, $S'_{\mathrm{d},ij,t}$ and $T^{-1}_{ij,t}$, respectively.

It is well accepted in the literature that the crystallographic misorientation of adjoining grains strongly influences the migration kinetics of the corresponding grain boundary [24,27,80]. Therefore, in the present section, we also investigate the influence of misorientation on the migration behavior. Note that the crystallographic orientation of lattice planes in a grain is specified relative to a chosen reference frame by a rotation matrix [81]. From 3DXRD image data, we obtain the local crystallographic orientation in each voxel of the measurement. For two grains that meet at a grain boundary G_{ij}, the difference in their orientations is quantified by the misorientation angle $\theta_{ij} \in [0, \pi)$, which denotes the (minimum) angle through which the lattice of one grain would need to be rotated to match the lattice of the other grain. A detailed description of how the misorientation angle is extracted from the orientation of two adjacent grains can be found in [81]. Accordingly, for each grain boundary point $p \in \widetilde{S}_{\mathrm{d},ij}$, the associated misorientation angle $\theta(p)$ is given by θ_{ij}. Because θ_{ij} has the same value at each point along the grain boundary G_{ij}, in addition to characterizing boundary migration in a pointwise manner in Section 5.1, we also analyze the migration of entire grain boundaries in Section 5.2.

5.1. **Local grain boundary migration**

Using the surface representation of the grain boundaries, the local mean curvature values $H_S(p)$, velocity values $v_{\mathrm{n}}(p)$ in normal direction and displacement angle values $\alpha(p)$ are computed for each point $p \in \widetilde{S}_{\mathrm{d},d_{\min}}$, whereby points less than $d_{\min} = 4$ from triple junctions are excluded, as described in Section 4.1. Here, the set $\widetilde{S}_{\mathrm{d},d_{\min}}$ is given by $\widetilde{S}_{\mathrm{d},d_{\min}} = \bigcup_{i,j \in \{1,\dots,n_G\}, i \neq j} T_{ij}(S'_{\mathrm{d},ij,d_{\min}})$, where $S'_{\mathrm{d},ij,d_{\min}}$ is given by Eq. (32) for the surface representation $S'_{\mathrm{d},ij}$. Figure 9 displays the relationship between these quantities as bivariate kernel density estimates [82]. The latter are shown in Figure 9(a) for $(H_S(p), \alpha(p))$ and in Figure 9(b) for $(H_S(p), v_{\mathrm{n}}(p))$ at each grain boundary point $p \in \widetilde{S}_{\mathrm{d},d_{\min}}$.

A potential relationship between $H_S(p)$ and $v_{\mathrm{n}}(p)$ is evaluated using the Pearson correlation coefficient (PCC) [83] and the empirical distance correlation coefficient (EDCC) [84]. The PCC is utilized to identify linear relationships, where a PCC value close to 1 or -1 indicates a strong linear relation, whereas a value close to 0 indicates little to no linear correlation. The EDCC is used to identify potential nonlinear relationships; in the case of two random variables, the EDCC equals zero if and only if these variables are independent, allowing for the detection of general (nonlinear) dependencies. For the quantities $H_S(p)$ and $v_{\mathrm{n}}(p)$, we obtained PCC and EDCC values of 0.04 and 0.0013, respectively.

In addition, a possible relationship between the grain boundary crystallography and the grain boundary itself is investigated with respect to the values of $v_{\mathrm{n}}(p)$ and $\theta(p)$ for all grain boundary points $p \in \widetilde{S}_{\mathrm{d},d_{\min}}$. Figure 10(a) displays violin and box plots of the values of $\theta(p)$ and $v_{\mathrm{n}}(p)$, using a bin width of 5° for the values of $\theta(p)$ for each box plot. Here, PCC and EDCC values of 0.09 and 0.21 were obtained for the values of $v_{\mathrm{n}}(p)$ and $\theta(p)$, respectively.

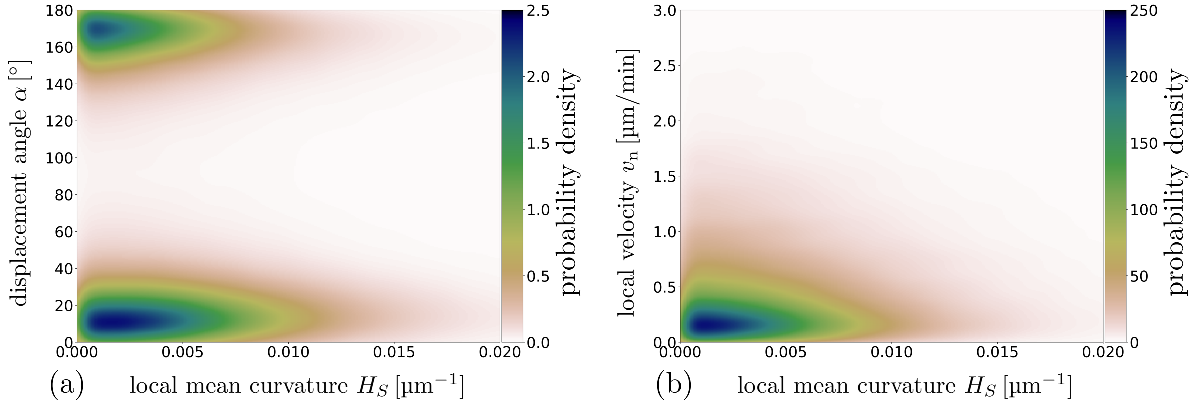

FIGURE 9. Bivariate kernel density estimates of the values of (a) local mean curvature and displacement angle $(H_S(p), \alpha(p))$, and (b) local velocity in normal direction and displacement angle $(v_{\mathrm{n}}(p), \alpha(p))$ for all grain boundary points $p \in \widetilde{S}_{\mathrm{d},d_{\min}}$, excluding points with distance less than $d_{\min} = 4$ from triple junctions.

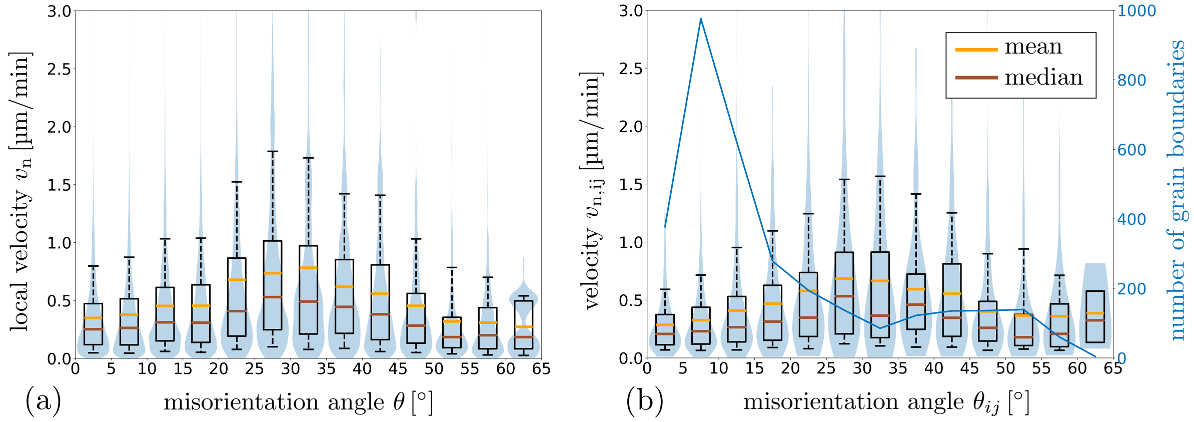

FIGURE 10. (a) Violin and box plots of local velocity values $v_{\mathrm{n}}(p)$ in normal direction against misorientation angles $\theta(p)$ for grain boundary points $p \in \widetilde{S}_{\mathrm{d},d_{\min}}$, excluding points less than $d_{\min} = 4$ from triple junctions. (b) Violin and box plots of mean local velocity values $v_{\mathrm{n},ij}$ in normal direction against misorientation angles θ_{ij} for all grain boundaries G_{ij}, where the number of grain boundaries in each bin is indicated by the blue curve. The boxes are bounded by the 25th and 75th percentiles, and the whiskers extend from the 10th to the 90th percentile. The mean and median values in each bin are marked by orange and brown lines, respectively.

5.2. Grain boundary migration

In addition to the pointwise characterizations of the previous section, we have also evaluated the migration behavior of entire grain boundaries. As described above, for each surface representation $\widetilde{S}_{\mathrm{d},ij,d_{\min}}$, the mean velocity $v_{\mathrm{n},ij} \in [0, \infty)$ in normal direction and standard deviation

$\sigma_{v_{\mathrm{n},ij}} \in [0,\infty)$ of the pointwise velocities of a given grain boundary are considered. The values of $v_{\mathrm{n},ij}$ and $\sigma_{v_{\mathrm{n},ij}}$ are given by

$$v_{\mathrm{n},ij} = \frac{1}{\#\widetilde{S}_{\mathrm{d},ij,d_{\min}}} \sum_{p\in\widetilde{S}_{\mathrm{d},ij,d_{\min}}} v_{\mathrm{n}}(p) \quad \text{and} \quad \sigma_{v_{\mathrm{n},ij}} = \sqrt{\frac{1}{\#\widetilde{S}_{\mathrm{d},ij,d_{\min}}} \sum_{p\in\widetilde{S}_{\mathrm{d},ij,d_{\min}}} (v_{\mathrm{n}}(p) - v_{\mathrm{n},ij})^2}. \tag{34}$$

Here, the coefficient of variation [85] of mean velocity, given by $\sigma_{v_{\mathrm{n},ij}}/v_{\mathrm{n},ij}$, indicates the extent of variability in relation to the mean velocity value for each grain boundary and is utilized as a descriptor for how uniformly a grain boundary migrates. More precisely, we judge a grain boundary to migrate rather uniformly if the value of $\sigma_{v_{\mathrm{n},ij}}/v_{\mathrm{n},ij}$ is small.

Furthermore, the mean curvature of each surface representation $\widetilde{S}_{\mathrm{d},ij,d_{\min}}$ is evaluated from the mean $\mu_{ij} \in [0,\infty)$ and standard deviation $\sigma_{ij} \in [0,\infty)$ of local mean curvature values $H_S(p)$ for all $p \in \widetilde{S}_{\mathrm{d},ij,d_{\min}}$, where μ_{ij} and σ_{ij} are given by

$$\mu_{ij} = \frac{1}{\#\widetilde{S}_{\mathrm{d},ij,t,d_{\min}}} \sum_{p\in\widetilde{S}_{\mathrm{d},ij,d_{\min}}} H_S(p) \quad \text{and} \quad \sigma_{ij} = \sqrt{\frac{1}{\#\widetilde{S}_{\mathrm{d},ij,d_{\min}}} \sum_{p\in\widetilde{S}_{\mathrm{d},ij,d_{\min}}} (H_S(p) - \mu_{ij})^2}. \tag{35}$$

Similar to the above, the coefficient of variation of local velocity — given by σ_{ij}/μ_{ij} — provides a descriptor of how irregularly a grain boundary is curved. We consider a grain boundary to be curved irregularly if it manifests a large variation in local mean curvature values and, therefore, a large ratio σ_{ij}/μ_{ij}.

Figures 11(a) and (b) display bivariate kernel density estimates of $(\mu_{ij}, \sigma_{ij}/\mu_{ij})$ and $(v_{\mathrm{n},ij}, \sigma_{v_{\mathrm{n},ij}}/v_{\mathrm{n},ij})$, obtained for each grain boundary with surface representation $\widetilde{S}_{\mathrm{d},ij,d_{\min}}$. Furthermore, a bivariate kernel density estimate of $(\mu_{ij}, v_{\mathrm{n},ij})$ is presented in Figure 11(c). In analogy to the investigation of local grain boundary migration, we also examine the relationship between crystallography and migration behavior of entire grain boundaries. Figure 10(b) displays violin and box plots of θ_{ij} and $v_{\mathrm{n},ij}$ values for each grain boundary with surface representation $\widetilde{S}_{\mathrm{d},ij,d_{\min}}$. Furthermore, the relationship between μ_{ij} and $v_{\mathrm{n},ij}$ is evaluated by computing the PCC and EDCC, yielding values of 0.07 and 0.0016, respectively. In contrast, for the quantities θ_{ij} and $v_{\mathrm{n},ij}$, the correlation coefficients PCC and EDCC are found to be 0.13 and 0.25, respectively.

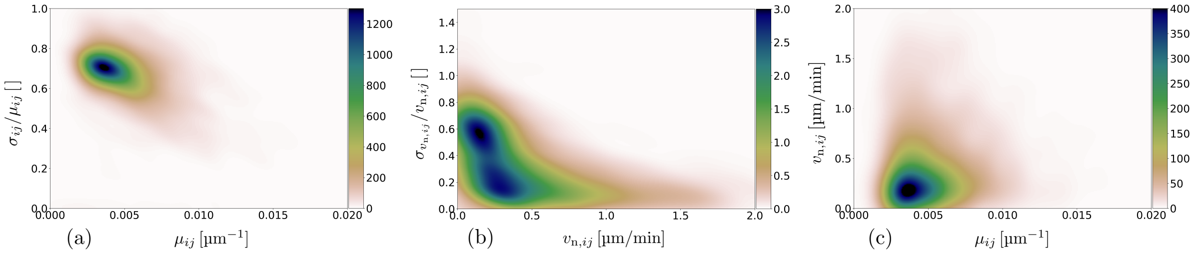

(a) (b) (c)

FIGURE 11. Bivariate kernel density estimates of (a) mean and coefficient of variation $(\mu_{ij}, \sigma_{ij}/\mu_{ij})$ of local mean curvature values, (b) mean and coefficient of variation $(v_{\mathrm{n},ij}, \sigma_{v_{\mathrm{n},ij}}/v_{\mathrm{n},ij})$ of local velocity values in normal direction, and (c) of $(\mu_{ij}, v_{\mathrm{n},ij})$ for all grain boundaries G_{ij} with surface representation $\widetilde{S}_{\mathrm{d},ij,d_{\min}}$, excluding points with distance less than $d_{\min} = 4$ from triple junctions.

5.3. **Discussion of migration results**

In this section, the results obtained for the AlMg dataset are discussed. In particular, the pointwise migration of grain boundaries is examined, with particular emphasis placed on the influence of local curvature and crystallographic orientation on the migration velocity. In addition, the relationship between the local migration behavior of individual boundary points and the overall migration of entire grain boundaries is investigated.

Local migration toward center of curvature. The results obtained from the surface representation method indicate that the assumption of grain boundary points migrating toward their local center of curvature does not generally hold, as a considerable fraction of points deviates from this behavior. This can be seen in the large displacement angles $\alpha(p)$ evident in Figure 9(a) for points $p \in \widetilde{S}_{\mathrm{d},d_{\min}}$. It should be noted that points with small local mean curvature values $H_S(p)$ are particularly sensitive to numerical errors in normal vector determination, which may lead to artificially large $\alpha(p)$ values. Nevertheless, approximately 78% of the points exhibit local mean curvature values greater than 0.002, and around 32% of these points are associated with $\alpha(p)$ values exceeding 90°.

Influence of curvature and crystallographic orientation on velocity. The results obtained indicate that the local mean curvature has almost no influence on the value of the local boundary velocity. For grain boundary points $p \in \widetilde{S}_{\mathrm{d},d_{\min}}$, no functional relationship is apparent between values of local mean curvature $H_S(p)$ and velocity $v_{\mathrm{n}}(p)$ in normal direction, as shown in Figure 9(b). This observation is supported by the PCC value of only 0.04. In addition, the EDCC value of $H_S(p)$ and $v_{\mathrm{n}}(p)$ equals 0.0013, further indicating the absence of a significant correlation between these two quantities. These findings suggest that, at the scale of individual grain boundary points, velocities in polycrystals are not proportional to the local mean curvature, in contrast to the fundamental assumption underlying Eq. (1). These results are comparable to those proposed in Refs. [46, 55, 56], where the authors investigate the influence of mean curvature on the migration of grain boundaries in Ni, $\mathrm{SrTiO_3}$ and Fe polycrystals. It should be noted that the cited studies assessed the relationship between velocity and mean curvature for grain boundaries considered as a whole, whereas our analysis cast doubt on the *local* validity of Eq. (1) — i.e., at individual points on a grain boundary. Nevertheless, our results indicate that the lattice misorientation of a grain boundary, quantified by the misorientation angle $\theta(p)$, has a noticeable influence on $v_{\mathrm{n}}(p)$. Although no linear relationship is detected between $\theta(p)$ and $v_{\mathrm{n}}(p)$ (as evidenced by a PCC value of 0.09), the EDCC value of 0.21 deviates significantly from zero, indicating the presence of a nonlinear relationship. This trend is consistent with Figure 10(a), where both the mean and median of $v_{\mathrm{n}}(p)$ increase with $\theta(p)$, reaching a maximum within the interval $[25°, 35°]$, followed by a decline at higher misorientation angles. When considering the combined influence of $H_S(p)$ and $\theta(p)$ on $v_{\mathrm{n}}(p)$, the EDCC value increases slightly to 0.25, suggesting a modest additional contribution of local mean curvature when coupled with crystallographic misorientation. These results are similar to those reported in Refs. [86] and [54], where the same AlMg dataset was analyzed to characterize the migration of entire grain boundaries.

Relation between local and entire grain boundary migration. The surface representation method provides detailed information regarding the local migration of grain boundary points. As outlined in Section 5.2, these local descriptors can be systematically aggregated to characterize the migration behavior of entire grain boundaries. The analysis carried out in the present paper shows that grain boundary representations $\widetilde{S}_{\mathrm{d},ij,d_{\min}}$ are generally flat, as reflected by their relatively small average curvature values μ_{ij}. The median value for μ_{ij} of only $0.0045\,\mathrm{\mu m^{-1}}$ is around 15 times smaller than the inverse of the specimen's average grain radius ($0.068\,\mathrm{\mu m^{-1}}$). At the same time, the comparatively large σ_{ij}/μ_{ij} values indicate that these boundaries exhibit significant variations in $H_S(p)$ across points $p \in \widetilde{S}_{\mathrm{d},ij,d_{\min}}$. In contrast, with respect to the velocities at various points on an individual grain boundary, the values of $\sigma_{v_{\mathrm{n},ij}}/\mu_{v_{\mathrm{n},ij}}$ are small in comparison to those of $\mu_{v_{\mathrm{n},ij}}$, indicating that nearly all points on a given grain boundary migrate at about the same speed, despite local curvature variations. This observation bolsters the interpretation that local curvature has little to no effect on the migration of grain boundaries considered as a whole. While a local geometric descriptors like mean curvature might influence boundary migration at very short length scales, the crystallographic relationships between neighboring grains and their general interconnected nature appears to have a stronger impact on the overall migration of grain boundaries in a polycrystal [56].

6. Conclusions

In this paper, we have developed a method for locally tracking grain boundaries in polycrystalline materials. Our approach enables the computation of mean curvature and velocity at individual points on a grain boundary directly from 3DXRD grain mappings. The method employs smoothing thin-plate splines to represent voxelized grain boundaries as continuous surfaces, allowing for the accurate evaluation of local quantities. Validation has been performed against a multiplicatively weighted Laguerre tessellation, which provides ground truth values for local mean curvature, as well as against a single-grain dataset (a Reuleaux tetrahedron) that was coarsened using a phase field simulation, furnishing known ground truth values for local velocity and reduced mobility. Furthermore, the applicability of the method was demonstrated on an experimental dataset exhibiting a complex grain architecture, for which the time-dependent migration of grain boundaries was analyzed. In the latter study, no clear correlation was identified between the local mean curvature of grain boundaries and the velocity of individual boundary points; however, the method did reveal significant correlations between the crystallographic misorientation at a grain boundary and both the local and boundary-averaged normal velocities. As such, the proposed method offers a robust framework for the extraction of grain growth kinetic data from time-resolved, voxelized mappings of grain boundary networks. Although previous approaches have been limited to determining boundary-averaged quantities, our method operates in a pointwise manner, thus providing a basis for identifying local grain boundary descriptors that may have previously unrecognized effects on boundary migration. In future work [87, 88], we plan to employ this method to assess the impact of second-phase particles on grain boundary migration during abnormal grain growth.

Data availability statement

The datasets generated and/or analyzed during the current study are available from the corresponding author on reasonable request.

Acknowledgment

This research is funded by the German Research Foundation (DFG) under project number 453092613 (KR 1658/9-1, SCHM 997/41-1).

References

[1] T. Sutoki. On the mechanism of crystal growth by annealing. Science Reports of the Tohoku Imperial University, 17:857–876, 1928.

[2] J. Burke and D. Turnbull. Recrystallization and grain growth. Progress in Metal Physics, 3:220–292, 1952.

[3] M.P. Anderson, G.S. Grest, and D.J. Srolovitz. Computer simulation of normal grain growth in three dimensions. Philosophical Magazine B, 59:293–329, 1989.

[4] M.P. Anderson, D.J. Srolovitz, G.S. Grest, and P.S. Sahni. Computer simulation of grain growth—–I. Kinetics. Acta Metallurgica, 32:783–791, 1984.

[5] M. Bernacki, R.E. Logé, and T. Coupez. Level set framework for the finite-element modelling of recrystallization and grain growth in polycrystalline materials. Scripta Materialia, 64:525–528, 2011.

[6] M. Elsey, S. Esedoglu, and P. Smereka. Diffusion generated motion for grain growth in two and three dimensions. Journal of Computational Physics, 228:8015–8033, 2009.

[7] D. Fan and L.Q. Chen. Computer simulation of grain growth using a continuum field model. Acta Materialia, 45:611–622, 1997.

[8] D. Fan, C. Geng, and L.Q. Chen. Computer simulation of topological evolution in 2-D grain growth using a continuum diffuse-interface field model. Acta Materialia, 45:1115–1126, 1997.

[9] K. Kawasaki, T. Nagai, and K. Nakashima. Vertex models for two-dimensional grain growth. Philosophical Magazine B, 60:399–421, 1989.

[10] C.E. Krill III and L.-Q. Chen. Computer simulation of 3-D grain growth using a phase-field model. Acta Materialia, 50:3059–3075, 2002.

[11] Y. Liu, T. Baudin, and R. Penelle. Simulation of normal grain growth by cellular automata. Acta Materialia, 34:1679–1683, 1996.

[12] M.A. Miodownik. A review of microstructural computer models used to simulate grain growth and recrystallisation in aluminium alloys. Journal of Light Metals, 2:125–135, 2002.

[13] I. Steinbach, F. Pezzolla, B. Nestler, M. Seeßelberg, R. Prieler, G.J. Schmitz, and J.L.L. Rezende. A phase field concept for multiphase systems. Physica D: Nonlinear Phenomena, 94:135–147, 1996.

[14] D. Weygand, Y. Bréchet, and J. Lépinoux. A vertex dynamics simulation of grain growth in two dimensions. Philosophical Magazine Part B, 78:329–352, 1998.

[15] E. Miyoshi, T. Takaki, M. Ohno, Y. Shibuta, S. Sakane, T. Shimokawabe, and T. Aoki. Ultra-large-scale phase-field simulation study of ideal grain growth. npj Computational Materials, 3:25, 2017.

[16] E. Miyoshi, T. Takaki, Y. Shibuta, S. Sakane, T. Shimokawabe, and T. Aoki. Correlation between three-dimensional and cross-sectional characteristics of ideal grain growth: large-scale phase-field simulation study. Journal of Materials Science, 53:15165–15180, 2018.

[17] B.L. Adams and T. Olson. The mesostructure—properties linkage in polycrystals. Progress in Materials Science, 43:1–87, 1998.

[18] M.A. Groeber, B.K. Haley, M.D. Uchic, D.M. Dimiduk, and S. Ghosh. 3D reconstruction and characterization of polycrystalline microstructures using a FIB–SEM system. Materials Characterization, 57:259–273, 2006.

[19] D.J. Rowenhorst, A.C. Lewis, and G. Spanos. Three-dimensional analysis of grain topology and interface curvature in a β-titanium alloy. Acta Materialia, 58:5511–5519, 2010.

[20] H.F. Poulsen. Three-Dimensional X-Ray Diffraction Microscopy: Mapping Polycrystals and Their Dynamics. Springer, 2004.

[21] M. McKenna, S.O. Poulsen, E.M. Lauridsen, W. Ludwig, and P.W. Voorhees. Grain growth in four dimensions: A comparison between simulation and experiment. Acta Materialia, 78:125–134, 2014.

[22] A. Bhattacharya, Y.F. Shen, C.M. Hefferan, S.F. Li, J. Lind, Suterm R.M., and G.S. Rohrer. Three-dimensional observations of grain volume changes during annealing of polycrystalline Ni. Acta Materialia, 167:40–50, 2019.

[23] J. Han, V. Vitek, and D.J. Srolovitz. Grain-boundary metastability and its statistical properties. Acta Materialia, 104:259–273, 2016.

[24] J. Humphreys, G.S. Rohrer, and A. Rollett. Recrystallization and Related Annealing Phenomena. Elsevier, 3rd edition, 2017.

[25] G. Gottstein and L.S. Shvindlerman. Grain Boundary Migration in Metals: Thermodynamics, Kinetics, Applications. CRC Press, 2010.

[26] G.S. Rohrer, D.M. Saylor, B. El Dasher, B.L. Adams, A.D. Rollett, and P. Wynblatt. The distribution of internal interfaces in polycrystals. Zeitschrift für Metallkunde, 95:197–214, 2004.

[27] G.S. Rohrer, I. Chesser, A.R. Krause, S.K. Naghibzadeh, Z. Xu, K. Dayal, and E.A. Holm. Grain Boundary Migration in Polycrystals. Annual Review of Materials Research, 53:347–369, 2023.

[28] G.S. Rohrer. Grain boundary energy anisotropy: A review. Journal of Materials Science, 46(18):5881–5895, 2011.

[29] V.V. Bulatov, B.W. Reed, and M. Kumar. Grain boundary energy function for fcc metals. Acta Materialia, 65:161–175, 2014.

[30] D.L. Olmsted, S.M. Foiles, and E.A. Holm. Survey of computed grain boundary properties in face-centered cubic metals: I. Grain boundary energy. Acta Materialia, 57:3694–3703, 2009.

[31] D.L. Olmsted, E.A. Holm, and S.M. Foiles. Survey of computed grain boundary properties in face-centered cubic metals—II: Grain boundary mobility. Acta Materialia, 57:3704–3713, 2009.

[32] S. Ratanaphan, D.L. Olmsted, V.V. Bulatov, E.A. Holm, A.D. Rollett, and G.S. Rohrer. Grain boundary energies in body-centered cubic metals. Acta Materialia, 88:346–354, 2015.

[33] M. Wang, S. Wu, and C.E. Krill III. Extraction of grain boundary curvature from voxel-based representations of polycrystalline microstructures. IOP Conference Series: Materials Science and Engineering, 580:012048, 2019.

[34] J.M. Dake, J. Oddershede, H.D. Sørensen, T. Werz, J.C. Shatto, K. Uesugi, S. Schmidt, and C.E. Krill III. Direct observation of grain rotations during coarsening of a semisolid Al–Cu alloy. Proceedings of the National Academy of Sciences, 113:E5998–E6006, 2016.

[35] S. Schmidt, S.F. Nielsen, C. Gundlach, L. Margulies, and D.J. Jensen. Watching the growth of bulk grains during recrystallization of deformed metals. Science, 305:229–232, 2004.

[36] S. Schmidt, U.L. Olsen, H.F. Poulsen, H.O. Sørensen, E.M. Lauridsen, L. Margulies, C. Maurice, and D. Juul Jensen. Direct observation of 3-D grain growth in Al-0.1%Mn. Scripta Materialia, 59:491–494, 2008.

[37] Z. Fan, Y. Wu, X. Zhao, and Y. Lu. Simulation of polycrystalline structure with Voronoi diagram in Laguerre geometry based on random closed packing of spheres. Computational Materials Science, 29:301–308, 2004.

[38] A. Lyckegaard, E.M. Lauridsen, W. Ludwig, R.W. Fonda, and H.F. Poulsen. On the use of Laguerre tessellations for representations of 3D grain structures. Advanced Engineering Materials, 13:165–170, 2011.

[39] A. Spettl, T. Brereton, Q. Duan, T. Werz, C.E. Krill III, D.P. Kroese, and V. Schmidt. Fitting Laguerre tessellation approximations to tomographic image data. Philosophical Magazine, 96:166–189, 2016.

[40] O. Šedivý, J.M. Dake, C.E. Krill III, and V. Schmidt. Description of the 3D morphology of grain boundaries in aluminium alloys using tessellation models generated by ellipsoids. Image Analysis & Setreology, 36:5–13, 2017.

[41] O. Šedivý, D. Westhoff, J. Kopeček, C.E. Krill III, and V. Schmidt. Data-driven selection of tessellation models describing polycrystalline microstructures. Journal of Statistical Physics, 172:1223–1246, 2018.

[42] R. Quey and L. Renversade. Optimal polyhedral description of 3D polycrystals: Method and application to statistical and synchrotron X-ray diffraction data. Computer Methods in Applied Mechanics and Engineering, 330:308–333, 2018.

[43] L. Petrich, O. Furat, M. Wang, C.E. Krill III, and V. Schmidt. Efficient fitting of 3D tessellations to curved polycrystalline grain boundaries. Frontiers in Materials, 8:760602, 2021.

[44] A. Okabe, B. Boots, K. Sugihara, and S.N. Chiu. Spatial Tessellations: Concepts and Applications of Voronoi Diagrams. J. Wiley & Sons, 2009.

[45] A. Alpers, O. Furat, C. Jung, M. Neumann, C. Redenbach, A. Saken, and V. Schmidt. Fitting generalized power diagrams to 3D image data: A prerequisite for virtual materials testing, 2025, Preprint (submitted).

[46] A. Bhattacharya, Y. Shen, C.M. Hefferan, S.F. Li, J. Lind, R.M. Suter, C.E. Krill III, and G.S. Rohrer. Grain boundary velocity and curvature are not correlated in Ni polycrystals. Science, 374:189–193, 2021.

[47] F.L. Bookstein. Principal warps: Thin-plate splines and the decomposition of deformations. IEEE Transactions on Pattern Analysis and Machine Intelligence, 11:567–585, 1989.

[48] W. Keller and A. Borkowski. Thin plate spline interpolation. Journal of Geodesy, 93:1251–1269, 2019.

[49] M.D. Buhmann. Radial Basis Functions: Theory and Implementations. Cambridge University Press, 2003.

[50] G.E. Fasshauer. Meshfree Approximation Methods with MATLAB. World Scientific, 2007.

[51] W.A. Light. Some aspects of radial basis function approximation. In S.P. Singh, editor, Approximation Theory, Spline Functions and Applications, pages 163–190. Springer, 1992.

[52] H. Wendland. Fast evaluation of radial basis functions: Methods based on partition of unity. In C.K. Chui, editor, Approximation Theory X: Wavelets, Splines, and Applications, pages 473–483. Vanderbilt University Press, 2002.

[53] F. Reuleaux. Theoretische Kinematik. Grundzüge einer Theorie des Maschinenwesens. Friedrich Vieweg und Sohn, 1875.

[54] J.M. Dake. Experimental Investigations of Microstructural Coarsening in 3D using X-Ray Microscopy. Phd thesis, Ulm University, 2020.

[55] V. Muralikrishnan, H. Liu, L. Yang, B. Conry, C.J. Marvel, M.P. Harmer, G.S. Rohrer, M.R. Tonks, R.M. Suter, C.E. Krill III, and A.R. Krause. Observations of unexpected grain boundary migration in SrTiO3. Scripta Materialia, 222:115055, 2023.

[56] Z. Xu, Y. Shen, S.K. Naghibzadeh, X. Peng, V. Muralikrishnan, S. Maddali, D. Menasche, A.R. Krause, K. Dayal, R.M. Suter, and G.S. Rohrer. Grain boundary migration in polycrystalline α-Fe. Acta Materialia, 264:119541, 2024.

[57] Z. Xu, J. Sun, J.M. Dake, J. Oddershede, H. Kaur, S.K. Naghibzadeh, C.E. Krill III, K. Dayal, and G.S. Rohrer. Grain boundary properties and microstructure evolution in an Al-Cu alloy. Acta Materialia, 292:121041, 2025.

[58] S.N. Chiu, D. Stoyan, W.S. Kendall, and J. Mecke. Stochastic Geometry and its Applications. J. Wiley & Sons, 3rd edition, 2013.

[59] A. Alpers, A. Brieden, P. Gritzmann, A. Lyckegaard, and H.F. Poulsen. Generalized balanced power diagrams for 3D representations of polycrystals. Philosophical Magazine, 95:1016–1028, 2015.

[60] R. Hynd. The surface area and volume of a reuleaux polyhedron. Journal of Computational Geometry, 16:35–64, 2025.

[61] A. Gray. Modern Differential Geometry of Curves and Surfaces with Mathematica. CRC Press, 2nd edition, 1998.

[62] P. Grinfeld. Introduction to Tensor Analysis and the Calculus of Moving Surfaces. Springer, 2013.

[63] A.I.R. Galarza and J. Seade. Introduction to Classical Geometries. Birkhäuser, 2007.

[64] J.M. McCarthy. Introduction to Theoretical Kinematics. MIT Press, 1990.

[65] T. Hastie, R. Tibshirani, and J. Friedman. The Elements of Statistical Learning. Springer, 2nd edition, 2009.

[66] H. Edelsbrunner, D.G. Kirkpatrick, and R. Seidel. On the shape of a set of points in the plane. IEEE Transactions on Information Theory, 29:551–559, 1983.

[67] N. Akkiraju, H. Edelsbrunner, M. Facello, P. Fu, E.P. Mucke, and C. Varela. Alpha shapes: Definition and software. In Proceedings of the 1st International Computational Geometry Software Workshop, volume 63, 1995.

[68] C. Gu and C. Gu. Smoothing Spline ANOVA Models. Springer, 2013.

[69] MATLAB. version 9.10.0.1649659 (R2021a). The MathWorks Inc., Natick, Massachusetts, 2021.

[70] X. Zhong, D.J. Rowenhorst, H. Beladi, and G.S. Rohrer. The five-parameter grain boundary curvature distribution in an austenitic and ferritic steel. Acta Materialia, 123:136–145, 2017.

[71] S. Hyde, B.W. Ninham, S. Andersson, K. Larsson, T. Landh, Z. Blum, and S. Lidin. The Language of Shape. Elsevier, 1997.

[72] S.J.P. Callens and A.A. Zadpoor. From flat sheets to curved geometries: Origami and kirigami approaches. Materials Today, 21:241–264, 2018.

[73] E. Vezzetti and F. Marcolin. Geometrical descriptors for human face morphological analysis and recognition. Robotics and Autonomous Systems, 60:928–939, 2012.

[74] R. Goldman. Curvature formulas for implicit curves and surfaces. Computer Aided Geometric Design, 22:632–658, 2005.

[75] R. Burkhard and E. Çela. Linear assignment problems and extensions. In Handbook of Combinatorial Optimization: Supplement Volume A, pages 75–149. Springer, 1999.

[76] S. Martello and P. Toth. Linear assignment problems. In S. Martello, G. Laporte, M. Minoux, and C. Ribeiro, editors, Surveys in Combinatorial Optimization, volume 132, pages 259–282. North-Holland, 1987.

[77] I.S. Duff and J. Koster. On algorithms for permuting large entries to the diagonal of a sparse matrix. SIAM Journal on Matrix Analysis and Applications, 22:973–996, 2001.

[78] S.G. Krantz and H.R. Parks. The Implicit Function Theorem: History, Theory, and Applications. Springer Science & Business Media, 2002.

[79] K. Schladitz, J. Ohser, and W. Nagel. Measuring intrinsic volumes in digital 3D images. In A. Kuba, L. Nyúl, and K. Palágyi, editors, 13th International Conference Discrete Geometry for Computer Imagery, pages 247–258. Springer, 2007.

[80] A.P. Sutton, E.P. Banks, and A.R. Warwick. The five-dimensional parameter space of grain boundaries. Proceedings of the Royal Society A, 471:20150442, 2015.

[81] V. Randle and O. Engler. Introduction to Texture Analysis: Macrotexture, Microtexture and Orientation Mapping. CRC Press, 2000.

[82] D.W. Scott. Multivariate Density Estimation: Theory, Practice, and Visualization. J. Wiley & Sons, 2015.

[83] J. Benesty, J. Chen, Y. Huang, and I. Cohen. Pearson correlation coefficient. In Noise Reduction in Speech Processing, volume 2, pages 1–4. Springer, 2009.

[84] G.J. Székely, M.L. Rizzo, and N.K.. Bakirov. Measuring and testing dependence by correlation of distances. The Annals of Statistics, 35:2769–2794, 2024.

[85] B.S. Everitt and A. Skrondal. The Cambridge Dictionary of Statistics, volume 4. Cambridge University Press, 2010.

[86] M. Wang. Reverse Engineering the Kinetics of Grain Growth in Al-based Polycrystals by Microstructural Mapping in 4D. Phd thesis, Ulm, University, 2022.

[87] A.H. Schulz-Harder, T. Wilhelm, J.M. Dake, K. Gutbrod, M. Atzen, M. Ziehmer, O. Furat, H. Fang, O.-P. Autran, W. Ludwig, V. Schmidt, and C.E. Krill III. Tracking the emergence and persistence of abnormal grain growth in the commercial aluminum alloy AA5252 using 3D X-ray microscopy. Working paper (under preparation).

[88] T. Wilhelm, A.H. Schulz-Harder, O. Furat, J.M. Dake, C.E. Krill III, and V. Schmidt. Analyzing the local influence of pinning particles on abnormal grain growth in polycrystalline materials. Working paper (under preparation).

[89] P. Gräfensteiner, J. Friebel, L. Ditscherlein, O. Furat, U.A. Peuker, and V. Schmidt. An AFM-based approach for quantification of guest particle deformation during mechano-fusion. Powder Technology, 434:119293, 2024.

[90] L. Hunyadi. Fitting quadratic curves and surfaces. `https://www.mathworks.com/matlabcentral/fileexchange/45356-fitting-quadratic-curves-and-surfaces`, Matlab Central File Exchange. Accessed March 25, 2025.

Appendix

A. Ellipsoid fitting

In this section, the heuristic approach for determining the optimal value $\widehat{\lambda}$ of the smoothing parameter λ in the surface representation (see Eq. (13) in Section 3.1) is outlined. This approach involves fitting an ellipsoid to the grain boundary of interest and selecting $\widehat{\lambda}$ such that the local mean curvature (as described in Section 3.2) of the fitted surface closely matches that of the ellipsoid. This ensures a sufficiently smooth surface while preserving the overall shape of the voxelized grain boundary derived from the image data. The fitting routine of an ellipsoid on voxelized image data closely follows the approach proposed in Ref. [89], where particle surfaces were modeled that had been measured via atomic force microscopy in a dry particle coating process.

Recall that the voxelized data of a grain boundary in the surface representation step are transformed such that the surface is aligned with the (x,y)-coordinate plane (see Section 3.1). The grain boundary is given by the set K_{xy} containing the x- and y-components of the transformed grain boundary voxel coordinates, and the set K_{z} contains the corresponding z-components. In this setting, the surface of an ellipsoid $E \subset \mathbb{R}^3$ is given by those points $p \in \mathbb{R}^3$ fulfilling the equation

$$(p - c_e)^\top Q^\top U Q (p - c_e) = 1, \tag{36}$$

where $c_e = (c_e^{(1)}, c_e^{(2)}, c_e^{(3)}) \in \mathbb{R}^3$ are the coordinates of its center, $U = \mathrm{diag}(u_1, u_2, u_3)$ is a diagonal 3×3 matrix whose diagonal entries $u_1, u_2, u_3 > 0$ are the lengths of its three semi-axes, and

$$Q = \begin{pmatrix} \cos(\gamma_1) & -\sin(\gamma_1) & 0 \\ \sin(\gamma_1) & \cos(\gamma_1) & 0 \\ 0 & 0 & 1 \end{pmatrix} \begin{pmatrix} \cos(\gamma_2) & 0 & \sin(\gamma_2) \\ 0 & 1 & 0 \\ -\sin(\gamma_2) & 0 & \cos(\gamma_2) \end{pmatrix} \begin{pmatrix} 1 & 0 & 0 \\ 0 & \cos(\gamma_3) & -\sin(\gamma_3) \\ 0 & \sin(\gamma_3) & \cos(\gamma_3) \end{pmatrix} \tag{37}$$

is a matrix that describes the rotation by angles $\gamma_1 \in [0, 2\pi)$,$\gamma_2 \in [0, 2\pi)$ and $\gamma_3 \in [0, 2\pi)$ about the z-, y- and x-axis, respectively. In order to determine the best-fit ellipsoid, a loss function $g\colon \mathbb{R}^3 \times (0, \infty)^3 \times [0, 2\pi)^3$ is considered, which is given by

$$g(c_e^{(1)}, c_e^{(2)}, c_e^{(3)}, u_1, u_2, u_3, \gamma_1, \gamma_2, \gamma_3) = \sum_{p_{\mathrm{z}} \in K_{\mathrm{z}}} \| p_{\mathrm{z}} - O_{\mathrm{z}}(p_{\mathrm{z}}) \|, \tag{38}$$

where $O_{\mathrm{z}}(p_{\mathrm{z}})$ is the orthogonal projection of $p_{\mathrm{z}} \in K_{\mathrm{z}}$ onto the surface of the ellipsoid described by Eq. (36). In order to compute $O_{\mathrm{z}}(p_{\mathrm{z}})$, the algorithm implemented in Ref. [90] is used. Minimizing the loss function g results in an ellipsoid $E \subset \mathbb{R}^3$ that best matches the grain boundary under consideration. In other words, this ellipsoid can be described explicitly by a function $e\colon K_{\mathrm{xy}} \to \mathbb{R}$ that maps each point $(p_{\mathrm{x}}, p_{\mathrm{y}}) \in K_{\mathrm{xy}}$ onto the surface of the ellipsoid E:

$$E = \{(p_{\mathrm{x}}, p_{\mathrm{y}}, e(p_{\mathrm{x}}, p_{\mathrm{y}})) \in K \times \mathbb{R} \colon (p_{\mathrm{x}}, p_{\mathrm{y}}, e(p_{\mathrm{x}}, p_{\mathrm{y}})) \text{ fulfills Eq. (36)}\}. \tag{39}$$

The representation of the ellipsoid $E \subset \mathbb{R}^3$ given in Eq. (39) enables computing the local mean curvature $H_E((p_{\mathrm{x}}, p_{\mathrm{y}}, e(p_{\mathrm{x}}, p_{\mathrm{y}}))$ for each point $(p_{\mathrm{x}}, p_{\mathrm{y}}) \in K_{\mathrm{xy}}$ using Eq. (15) of Section 3.2, where, instead of the surface representation S with surface function s, the set E with surface function e is used.

The optimal value $\widehat{\lambda}$ of the smoothing parameter λ introduced in Eq. (13) is then computed for a surface representation S with surface function s_w by

$$\widehat{\lambda} = \operatorname*{arg\,min}_{\lambda \in [0,1]} \sum_{(p_{\mathrm{x}}, p_{\mathrm{y}}) \in K_{\mathrm{xy}}} \| H_S((p_{\mathrm{x}}, p_{\mathrm{y}}, s_w(p_{\mathrm{x}}, p_{\mathrm{y}}))) - H_E((p_{\mathrm{x}}, p_{\mathrm{y}}, e(p_{\mathrm{x}}, p_{\mathrm{y}}))) \|. \tag{40}$$

B. **Phase field simulation**

In Section 4.2, a three-dimensional phase field algorithm [10] was applied to a Reuleaux tetrahedron with faces having a radius of 80 voxels. The phase field model reproduces the conventional model of curvature-driven grain boundary migration proposed by Burke and Turnbull [2], in which a grain boundary migrates with local velocity defined by Eq. (1). Since we employ an isotropic simulation, each grain boundary evolves with the same reduced mobility $\widetilde{M} = M\gamma$, and the velocity of each grain boundary at time $t \in [0, \infty)$ can be expressed as

$$v_t = \widetilde{M} H_t. \tag{41}$$

The configuration of grain boundaries generated by the phase field algorithm was repeatedly recorded as image data once a fixed number of iterations had been carried out, introducing a discretization step that renders the simulation results comparable to experimental image data. The grain boundary mobility M and the excess energy γ are not direct inputs to our model but rather defined implicitly by the phenomenological parameters of the simulation. In order to determine the reduced mobility while also taking into account the effects of discretization, the phase field algorithm was first applied to a sphere. The advantage of considering a spherical grain is that its evolution under Eq. (1) can be computed analytically; consequently, the value of $\widetilde{M}_t$ at each time $t \in [0, \infty)$ is given by

$$\widetilde{M}_t = \frac{V_{\mathrm{vol},0}^{\frac{2}{3}} - V_{\mathrm{vol},t}^{\frac{2}{3}}}{2(\frac{4}{3}\pi)^{\frac{2}{3}} t}, \tag{42}$$

where $V_{\mathrm{vol},0}$ and $V_{\mathrm{vol},t}$ are the volumes of the sphere at times 0 and t, respectively. For additional details on the phase field simulation, readers are referred to Ref. [86].

To determine the value of the reduced mobility in the discretized image data, denoted by $\widetilde{M}_{\mathrm{d}}$, 10 000 iterations of the phase field algorithm were performed on a spherical grain with an initial radius of 80. The simulation results were recorded as image data every 200 iterations, yielding time-resolved images at time steps $t \in \{0, 200, 400, \ldots, 10000\}$. The value of $\widetilde{M}_{\mathrm{d}}$ was then obtained from Eq. (42), where, for each time step t, the initial and current volumes, $V_{\mathrm{vol},0}$ and $V_{\mathrm{vol},t}$, are computed from the image data by counting the voxels belonging to the sphere. Assuming a constant grain boundary mobility during the simulation, $\widetilde{M}_{\mathrm{d}}$ was computed as the mean of $\widetilde{M}_t$ over all recorded time steps, resulting in $\widetilde{M}_{\mathrm{d}} = 0.295$.

Since the grain boundaries of the Reuleaux tetrahedron correspond to spherical patches, their migration behavior is similar to that of the boundaries of the respective spheres. Consequently, when the phase field algorithm is applied using the same setup as for the spherical case above, we can assume that the grain boundaries of the Reuleaux tetrahedron migrate with the same reduced mobility $\widetilde{M}_{\mathrm{d}} = 0.295$. We carried out 2400 iterations of the phase field algorithm on the initial Reuleaux tetrahedron with radius $r = 80$, where after every 200 iterations the results obtained by the algorithm were recorded. As a result, time-resolved image data of the Reuleaux tetrahedron are available at the simulation steps $t \in \{0, 200, 400, \ldots, 2400\}$, with a time-step length Δt of 200 iterations. Furthermore, assuming that at each iteration of the phase field algorithm the resulting body obtained from the time-resolved image data remains a Reuleaux tetrahedron, each grain boundary point of the Reuleaux tetrahedron at a given simulation step $t \in \{0, 200, 400, \ldots, 2400\}$ has a Euclidean distance of $r_t > 0$ from the center of the corresponding sphere, as described in Section 2.1.2. More precisely, the radius r_t can be computed from image data using the following formula provided in Ref. [60]:

$$r_t = \sqrt[3]{\frac{12 V_{\mathrm{vol},t}}{3\sqrt{2} + 32\pi + 81\cos^{-1}(1/3)}}\ , \tag{43}$$

where $V_{\mathrm{vol},t} \in [0, \infty)$ denotes the volume of the voxelized representation of the Reuleaux tetrahedron at simulation step t, obtained by voxel counting. Consequently, at each simulation step $t \in \{0, 200, 400, \ldots, 2400\}$ of the phase field algorithm, each grain boundary point has a local mean curvature $H_t = 1/r_t$.

However, in order to obtain ground truth values for the grain boundary velocity from the image data — to which the results of the proposed surface representation method can be compared — two aspects must be addressed. First, only the output of the phase field algorithm at iterations $t \in \{0, 800, 1600, 2400\}$ with a time-step length of $\Delta t = 800$ are considered for model validation, as this interval corresponds to a sufficient number of iterations for noticeable grain boundary migration to occur. Second, the simulation does not give us the velocity of a grain boundary at any given time step t; rather, the velocity must be computed from the evolution of microstructure that occurs during Δt. As the Reuleaux tetrahedron shrinks in size, the mean curvature of its faces increases. The average boundary velocity between time steps t and $t + \Delta t$, $v_{t,t+\Delta t}$ can be computed from the time-averaged mean curvature $H_{t,t+\Delta t}$ according to

$$v_{\mathrm{d},t,t+\Delta t} = \widetilde{M} H_{t,t+\Delta t},$$

where $H_{t,t+\Delta t}$ is given by

$$H_{t,t+\Delta t} = \frac{1}{n_{t,t+\Delta t}} \sum_{i=1}^{n_{t,t+\Delta t}} H_{t_i}.$$

Here, t_i for $i \in \{1, 2, \ldots, n_{t,t+\Delta t}\}$ denote intermediate time steps between t and $t + \Delta t$, with $t_0 = t$, $t_{n_{t,t+\Delta t}} = t + \Delta t$ and $n_{t,t+\Delta t} > 0$. Note that for computing $v_{\mathrm{d},t,t+\Delta t}$ at time steps $t \in \{0, 800, 1600, 2400\}$ all available outputs of the phase field algorithm at iterations $0, 200, 400, \ldots, 2400$ are considered. For example, the value of $H_{0,800}$ between time step 0 and 800 is given by $H_{0,800} = \frac{1}{5}(H_0 + H_{200} + H_{400} + H_{600} + H_{800})$, where H_{t_i} is computed by $H_{t_i} = 1/r_{t_i}$ and r_{t_i} is given by Eq. (43). Furthermore, each point on the boundary of the Reuleaux tetrahedron undergoes a displacement $d_{\mathrm{d},t,t+\Delta t}$ given by $d_{\mathrm{d},t,t+\Delta t} = v_{\mathrm{d},t,t+\Delta t} \Delta t$.

To summarize, the values of reduced mobility $\widetilde{M}_{\mathrm{d}}$, mean curvature H_t, velocity $v_{\mathrm{d},t,t+\Delta t}$ and displacement $d_{\mathrm{d},t,t+\Delta t}$ obtained at a given simulation step $t \in \{0, 800, 1600, 2400\}$ with $\Delta t = 800$ serve as ground truth values for validation of the surface representation model introduced in Section 3. The superscript $*$ is used when referring to these ground truth values: i.e., we write $\widetilde{M}^*$, H_t^*, v_t^*, d_t^*, instead of $\widetilde{M}_{\mathrm{d}}$, H_t, $v_{\mathrm{d},t,t+\Delta t}$, $d_{\mathrm{d},t,t+\Delta t}$, respectively.

C. List of Symbols

grain boundary migration		**image data**	
symbol	description	symbol	description
v	velocity	I	image
M	mobility	W	image domain
H	mean curvature	W'	sampling window
γ	excess energy	n_G	number of grains observed in an image
θ	misorientation angle	G_i	set of voxels belonging to the ith grain
$\widetilde{M}$	reduced mobility	G_{ij}	set of voxels belonging to the grain boundary of ith and jth grain
t	time		
Δt	timestep	$I_{G_{ij}}$	binary image of G_{ij}
p	grain boundary point	$D_j(x)$	neighborhood of x within grain G_j
D	displacement vector	$n_{G_{ij}}$	number of voxels in G_{ij}
d	pointwise displacement	J_{ij}	set of voxels belonging to the triple junctions of G_{ij}
V	velocity vector		
N	normal vector field		
α	displacement angle		
multiplicatively weighted Laguerre tessellation		**Reuleaux tetrahedron**	
$\mathcal{T}$	tessellation	R	set of points belonging to the Reuleaux tetrahedron
$\mathcal{T}_\mathrm{d}$	discretized version of $\mathcal{T}$		
$I_{\mathcal{T}_\mathrm{d}}$	image of $\mathcal{T}_\mathrm{d}$	s_i	ith sphere center that generates R
C_i	ith cell	r	radius of the spheres
C_{ij}	facet of ith and jth adjacent cell	R_i	ith grain boundary
$C_{\mathrm{d},i}$	discretized version of C_i	R_d	discretized version of R
$n_{\mathcal{T}}$	number of tessellation cells	I_{R_d}	image of R_d
$\mathcal{G}$	marked point pattern	r_t	radius of Reuleaux tetrahedron at time t
g_i	ith seed point of $\mathcal{G}$		
m_i	ith multiplicate weight of $\mathcal{G}$		
a_i	ith additive weight of $\mathcal{G}$		
surface representation method		**exchanged volume method**	
T	rigid transformation	V_vol	volume
K_xy	(x,y)-components of transformed grain boundary voxel coordinates	V_ex	exchanged volume
		v_ex	grain boundary velocity by means of exchanged volume method
K_z	z-components of transformed grain boundary voxel coordinates	S_A	grain boundary surface area
S	surface representation	$\widetilde{M}_\mathrm{ex}$	reduced mobility by means of exchanged volume method
s	surface function of S		
A	domain of s		
s_w	parametric approximation of s		
w	parameter vector of s_w		
φ	thin plate spline		
λ	smoothing parameter		
L	surface roughness control function		
N_S	normal vector field of S		
H	local mean curvature regarding N_S		

model validation and results

symbol	description
δ	pointwise measure for accuracy of fitted surface representation
$\varepsilon_{\mathrm{rel}}$	pointwise relative error of mean curvature computation
$d_{\min}$	minimal distance of points to triple junctions
$v_{\mathrm{n},ij}$	mean of normal velocity values of points on grain boundary G_{ij}
$\sigma_{v_{\mathrm{n}},ij}$	standard deviation of normal velocity values of points on grain boundary G_{ij}
μ_{ij}	mean of local mean curvature values of points on grain boundary G_{ij}
σ_{ij}	standard deviation of local mean curvature values of points on grain boundary G_{ij}

index

symbol	description
v_n	descriptor v in normal direction
S_t	surface representation at time t
S_{d}	discretized version of surface representation S
S_{ij}	surface representation of grain boundary G_{ij}
$S_{ij,d_{\min}}$	points in S_{ij} with at least a distance of $d_{\min}$ away from triple junctions J_{ij}
H^*	ground truth value of descriptor H